

AD/A-000 025

AN INTERFEROMETRIC INVESTIGATION OF  
SHOCK STRUCTURE AND ITS INDUCED  
SHOCK-TUBE BOUNDARY LAYER IN IONIZED  
ARGON

Peter I. Brimelo, et al

Toronto University

Prepared for:

Air Force Office of Scientific Research

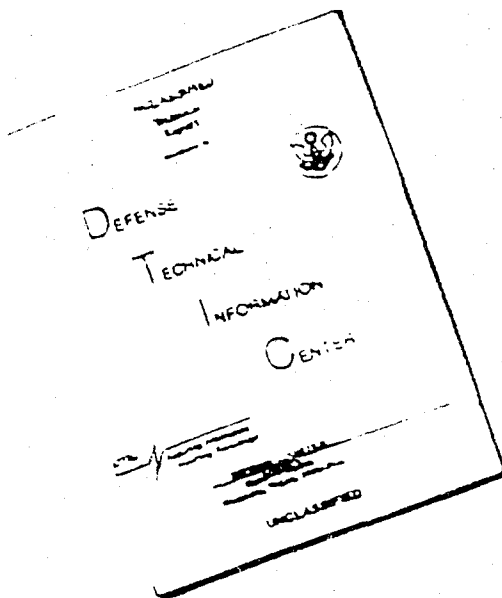
July 1974

DISTRIBUTED BY:



National Technical Information Service  
U. S. DEPARTMENT OF COMMERCE

# **DISCLAIMER NOTICE**



THIS DOCUMENT IS BEST  
QUALITY AVAILABLE. THE COPY  
FURNISHED TO DTIC CONTAINED  
A SIGNIFICANT NUMBER OF  
PAGES WHICH DO NOT  
REPRODUCE LEGIBLY.

UNCLASSIFIED

~~-SECURITY CLASSIFICATION OF THIS PAGE WHEN DATA ENTERED~~

**DD FORM 1473 JAN 73** EDITION OF 1 NOV 68 IS OBSOLETE

UNCLASSIFIED

SECURITY CLASSIFICATION OF THIS PAGE (If any) (Other Data Entered)

**UNCLASSIFIED**

**SECURITY CLASSIFICATION OF THIS DOCUMENT IS UNCHANGED**

of collision theory. In the nonequilibrium relaxation region a much faster ionization rate than in the free stream was found near the wall. This phenomenon has not been explained. Boundary layer density and degree of ionization profiles at 4cm and 20cm behind a shock wave of Mach number 16.5 indicate a laminar boundary layer growing from 0.7mm to 2mm in thickness. Similar profiles are presented for a station 10cm behind a shock wave of Mach number 13.5. The profiles are in better agreement with analysis for frozen or nonequilibrium boundary layers than for equilibrium profiles.

*ja* **UNCLASSIFIED**

**SECURITY CLASSIFICATION OF THIS DOCUMENT IS UNCHANGED**

AN INTERFEROMETRIC INVESTIGATION OF SHOCK  
STRUCTURE AND ITS INDUCED SHOCK-TUBE  
BOUNDARY LAYER IN IONIZED ARGON

by

Peter I. Brimelow

Manuscript received July, 1974.



July, 1974.

UTIAS Technical Note No.187  
CN ISSN 0082-5263

if

Acknowledgements

The guidance and supervision afforded by Dr. I. I. Glass in the course of my Masters degree program is very gratefully acknowledged.

I wish to extend sincere thanks to Mr. B. T. Whitten whose helpful advice and assistance in every aspect of this research project was invaluable in its successful completion.

The technical assistance given by Mr. P. Crouse during the experimental program is greatly appreciated.

I should like to thank Dr. W. S. Liu for providing the theoretical results presented in this report.

The financial assistance received from the Air Force Office of Scientific Research under Grant No. ~~✓~~-AFOSR-72-2274B and from the National Research Council of Canada is acknowledged with thanks.

### Summary

The structure of ionizing shock waves and their induced boundary layers in argon have been studied experimentally in the UTIAS 4" x 7" hypervelocity shock tube using dual-wavelength interferometry.

The relaxation lengths and transitions of shocks of Mach numbers 16.5 and 13.5 for initial gas pressures of about 5 torr have been measured at 2 cm and 8 cm, respectively. The transition profiles and relaxation lengths are in reasonably good agreement with analysis.

The effect of 0.4% hydrogen addition to the argon test gas for the stronger shock case is a reduced relaxation length from 20 mm to 6 mm, which can be explained on the basis of collision theory.

In the nonequilibrium relaxation region a much faster ionization rate than in the free stream was found near the wall. This phenomenon has not been explained.

Boundary layer density and degree of ionization profiles at 4 cm and 20 cm behind a shock wave of Mach number 16.5 indicate a laminar boundary layer growing from 0.7 mm to 2 mm in thickness. Similar profiles are presented for a station 10 cm behind a shock wave of Mach number 13.5.

The profiles are in better agreement with analysis for frozen or non-equilibrium boundary layers than for equilibrium profiles.

Table of Contents

	<u>Page</u>
Acknowledgements	ii
Summary	iii
Notation	v
1. INTRODUCTION	1
2. ANALYSIS	2
2.1 Free stream Relaxation Region	2
2.2 Equilibrium Boundary Layer	5
3. DESCRIPTION OF EXPERIMENTAL EQUIPMENT AND TECHNIQUES	8
3.1 The Shock Tube	8
3.2 Shock Velocity Measurement	10
3.3 Optics	10
3.3.1 Light Source	10
3.3.2 Mach-Zehnder Interferometer	11
3.3.3 Interferogram Photography	11
3.3.4 Test Section Plane of Focus	12
4. RESULTS AND DISCUSSION	13
4.1 Shock Front	13
4.2 Free stream Relaxation Region	14
4.3 Wall Effects in Relaxation Region	16
4.4 Boundary Layer	17
5. CONCLUSIONS	19
References	21
Figures	
APPENDICES:	
Appendix A: Thermodynamic and Transport Properties of Partially Ionized Argon	
"      B: Alignment of Interferometer and Light Source	
"      C: Analysis of Interferograms	

Notation

a	speed of sound
A	shock tube cross-sectional area, argon atom
c <sub>p</sub>	specific heat (constant pressure)
c <sub>v</sub>	specific heat (constant volume)
D <sub>A</sub>	ambipolar diffusion coefficient
h <sub>I</sub>	ion enthalpy
h	enthalpy
H	total enthalpy
k	Boltzmann constant
K	thermal conductivity
Le	Lewis number
m	mass
M	Mach number
n	particle number density
p, P	pressure
Pr	Prandtl number
Q	collision cross-section
R	gas constant
Sc	Schmidt number
t	time
u	particle velocity in x-direction
u <sub>s</sub>	shock velocity
v	particle velocity in y-direction
ẇ	species net production rate
x	streamwise direction
y	co-ordinate direction perpendicular to wall
α	degree of ionization

## 1. INTRODUCTION

In recent years much effort has been devoted to the study of hot gas flows, where the presence of atoms, ions and electrons as separate species in the gas considerably complicates the physical mechanisms involved in the flow. Therefore, an understanding of the behaviour of the different species and their interactions with each other has become essential in predicting the fluid properties of hot gas flows.

The relevance of such research to present-day requirements is as great as ever with the development of such vehicles as the space shuttle. A knowledge of the physical characteristics of dissociated and ionized gas flows is important not only for the design of such vehicles that must withstand re-entry conditions, where temperatures caused by shock and viscous heating are of sufficient magnitude to make dissociation and ionization effects significant, but also for the test facilities that are used to simulate suitable flight conditions for these spacecraft.

The shock tube is one such facility which is capable of generating high temperature, high Mach number gas flows in which dissociation and ionization processes take place. The UTIAS 4" x 7" hypervelocity shock tube, which was used for this experimental study, is capable of very high performance, generating shock Mach numbers in excess of 24 in argon gas. The relatively large cross-sectional area of this shock tube makes it especially suitable for the study of boundary layers, the effect of which on the free-stream is virtually negligible.

Argon is chosen as a test gas for a number of reasons. It is a monoatomic gas and consequently dissociation effects are eliminated, which simplifies the experimental technique, as will be seen later. Argon has a relatively low first ionization potential (15.7 eV) compared to some other monoatomic gases, which practically speaking means that for a given set of initial conditions a higher degree of ionization is achieved than for a gas of higher potential. The thermodynamic and transport properties of argon have been well established over a wide range of temperatures and pressures. Lastly, argon is available commercially and relatively cheaply with a high degree of purity and it is a safe gas to work with.

The experimental study described in this report was originally intended to investigate only the shock-tube wall boundary layer formed behind ionizing shock waves. However, it soon became apparent that the optical system which was set up to study the thin boundary layer region was equally suited to studying the shock-wave structure with which it initially interacts.

In the literature many theoretical analyses have been presented describing the structure of ionizing shock waves (e.g., Refs. 1-4) and also some on nonstationary ionized boundary layers (Refs. 5-7) but very little has been reported on experimental results obtained in the areas of interest here. References 4, 8 and 9 give some experimental results obtained for the boundary layer region while Refs. 3 and 10 give some experimental profiles for the shock wave relaxation region.

## 2. ANALYSIS

The theoretical analyses presented in this section are not meant to be complete treatments of the problems, but more as an outline of the relevant equations and factors which are important in obtaining a general solution.

The flow regions may be separated into distinct sections as follows (Fig. 1). In the freestream the Rankine-Hugoniot shock front, behind which the flow is frozen, is followed by nonequilibrium flow during which energy equilibration (or relaxation) processes take place. The chemical kinetics involved in this region are discussed later. Behind the relaxation region the gas is in thermochemical equilibrium, although some changes do take place slowly due to radiation losses. The viscous boundary layer growth begins at the shock front and extends back through the nonequilibrium flow region into the equilibrium flow region. The theoretical boundary layer analysis presented in Sec. 2.2 is limited to the equilibrium boundary layer problem.

### 2.1 Freestream Relaxation Region

The governing equations of mass, momentum and energy written for one-dimensional steady state flow in the shock-wave region are (Refs. 11 and 12)

$$\frac{d}{dx} (\rho u) = 0 \quad (2.1.1)$$

$$\frac{d}{dx} \left( \rho u^2 + p - \frac{4}{3} \mu \frac{du}{dx} \right) = 0 \quad (2.1.2)$$

$$\rho u \frac{dT}{dx} + p \frac{du}{dx} = \frac{4}{3} \mu \left( \frac{du}{dx} \right)^2 + \frac{d}{dx} \left( K \frac{dT}{dx} \right) \quad (2.1.3)$$

The momentum equation (Eq. 2.1.2) is derived from the Navier-Stokes equations. The  $4/3 \mu$  coefficient arises from Stokes' assumption that the second coefficient of viscosity  $\lambda = -2\mu/3$  and noting that for a monatomic gas the coefficient of bulk viscosity is zero.

The terms on the right-hand side of the energy equation (Eq. 2.1.3) describe entropy production in the shock wave.

Equations 2.1.1, 2.1.2 and 2.1.3 describe the flow both through the shock front (translational excitement only) and through the ensuing relaxation region. In the former region (layer) the gradients in the flow variables are large and the effects of viscosity and heat conduction must be considered. In this analysis we shall be concerned only with the relaxation region and since the gradients in flow properties are not large, the viscous and heat conduction dissipative processes may be neglected. Thus Eqs. 2.1.1, 2.1.2 and 2.1.3 may be reduced to take the following form:

$$\frac{d}{dx} (\rho u) = 0 \quad (2.1.4)$$

$$\rho u \frac{du}{dx} + \frac{dp}{dx} = 0 \quad (2.1.5)$$

$$\rho \frac{dh}{dx} - \frac{dp}{dx} = 0 \quad (2.1.6)$$

which when integrated yield the standard equations (Ref. 13)

$$\rho u = \rho_1 u_1 \quad (2.1.7)$$

$$p + \rho u^2 = p_1 + \rho_1 u_1^2 \quad (2.1.8)$$

$$h + \frac{1}{2} u^2 = h_1 + \frac{1}{2} u_1^2 \quad (2.1.9)$$

where  $u$  and  $u_1$  are measured relative to the fixed shock front.

Following Ref. 1, Eqs. 2.1.7, 2.1.8 and 2.1.9 together with the two-temperature concept in the equation of state (for the electrons and heavy particles)

$$p = \rho R (T + \alpha T_e) \quad (2.1.10)$$

and enthalpy equation

$$h = 5/2 R (T + \alpha T_e) + \alpha R \theta_I \quad (2.1.11)$$

are solved to give the particle velocity (assumed the same for heavy particle and electron alike)

$$u = \frac{u_s}{8} \left\{ 5 + \frac{3}{M_s^2} \pm \left[ 9 \left( 1 - \frac{1}{M_s^2} \right)^2 + \frac{96\alpha}{5M_s^2} \frac{\theta_I}{T_1} \right]^{1/2} \right\} \quad (2.1.12)$$

where the negative sign gives the physically meaningful result and  $M_s$ , the shock Mach number is defined as

$$M_s = u_s / (5/3 R T_1)^{1/2} = u_s / a_1$$

The gas temperature  $T$  is

$$T = T_1 \left\{ 1 - \alpha \left( \frac{T_e}{T_1} \right) - \frac{2}{5} \alpha \left( \frac{\theta_I}{T_1} \right) + \frac{M_s^2}{3} \left[ 1 - \left( \frac{u}{u_s} \right)^2 \right] \right\} \quad (2.1.13)$$

To determine the degree of ionization,  $\alpha$  and electron temperature  $T_e$ , we now consider the mass and energy conservation equations for the electron gas

$$\begin{aligned}\frac{d}{dx} (n_e u) &= \dot{n}_e \\ n_e u \frac{d}{dx} (3/2 k T_e) + n_e k T_e \frac{du}{dx} &= 3n_e \left( \frac{m_e}{m_A} \right) (\nu_{eA} + \nu_{eI}) k (T - T_e) - (\dot{n}_e) k (\theta_I + 3/2 T_e) - \frac{2}{3} \frac{T_e}{u} \frac{du}{dx}\end{aligned}\quad (2.1.14)$$

where  $x$  is the streamwise co-ordinate and  $\nu_{eA}, \nu_{eI}$  are the elastic collision frequencies for electron-atom and electron-ion collisions respectively and are related to the corresponding elastic collision cross-sections as (Ref. 2)

$$\begin{aligned}\nu_{eA} &= \frac{4(1-\alpha)\rho}{3 m_a} \left( \frac{8 k T_e}{\pi m_e} \right)^{1/2} Q_{eA} \\ \nu_{eI} &= \frac{\alpha\rho}{m_a} \left( \frac{8 k T_e}{\pi m_e} \right)^{1/2} Q_{eI}\end{aligned}\quad (2.1.15)$$

Equations (2.1.14) may be written in terms of the degree of ionization  $\alpha$ , as

$$\begin{aligned}u \frac{d\alpha}{dx} &= \dot{\alpha} = \dot{\alpha}_A + \dot{\alpha}_e \\ 3/2 u \frac{dT_e}{dx} + T_e \frac{du}{dx} &= 3 \left( \frac{m_e}{m_A} \right) (\nu_{eA} + \nu_{eI}) (T - T_e) - \frac{\dot{\alpha}_e}{\alpha^2} \theta_I\end{aligned}\quad (2.1.16)$$

where  $\dot{\alpha}_A$  and  $\dot{\alpha}_e$  are the ionization rates due to atom-atom and atom-electron collisions, respectively. Then

$$\frac{d\alpha}{dx} = \dot{\alpha}/u \quad (2.1.17)$$

and

$$\frac{dT_e}{dx} = 2 \left( \frac{m_e}{m_A} \right) \frac{\nu_{eA} + \nu_{eI}}{u} (T - T_e) - \frac{2}{3} \frac{\dot{\alpha}_e}{\alpha} \frac{\theta_I}{u} \quad (2.1.18)$$

If the local steady state approximation is assumed, i.e.,  $dT_e/dx \approx 0$ , then Eq. 2.1.18 gives

$$T_e = T - \frac{1}{3} \left( \frac{m_A}{m_e} \right) \frac{(\theta_I + 3/2 T_e)}{\nu_{eA} + \nu_{eI}} \left( \frac{\dot{\alpha}_e}{\alpha} \right) \quad (2.1.19)$$

where  $\dot{\alpha}_e$ ,  $v_{eA}$  and  $v_{eI}$  are all functions of  $T_e$  (see Ref. 1 for  $\dot{\alpha}_e$ ).

In principle, Eqs. 2.1.17 and 2.1.18 or Eqs. 2.1.17 and 2.1.19 may be solved numerically to give  $\alpha$  and  $T_e$  for given  $x$ , although the boundary conditions for  $T_e$  require careful consideration.

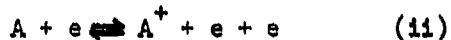
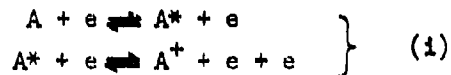
The chemical kinetic theory describing the processes in a shock wave leading to excitation and ionization has been discussed by a number of authors (e.g., Refs. 1,3,4). A simple outline is given here of the more popular theory which involves a two-step atom-atom collision process followed by a two-step electron-atom and single-step electron-electron collisional model (see Fig. 1).

With the initial discontinuous jump in flow conditions having taken place through the Rankine-Hugoniot shock front (whose thickness is of the order of a few mean free path lengths), the gas is in a frozen state, the energy transfer taking place only in the translational mode. The relaxation region begins with a two-step atom-atom collisional process



which takes some atoms to their first excited state before further collisions energize them sufficiently to free the electron. This relatively slow, inefficient process leads to the production of a small number of electrons.

The next phase is characterized by a two-step and a single-step event by which the energy transfer rate is considerably speeded up.



The latter process soon predominates, leading to the rapid production of electrons until an equilibrium state is reached with electrons recombining at the same rate at which they are produced. This balance is somewhat disturbed by radiative cooling by which some energy is lost through the emission of radiation, with a consequent drop in electron number density. This process affects the entire flow uniformity behind the shock front.

## 2.2 Equilibrium Boundary Layer

The boundary layer formed behind a normal shock wave travelling along an infinite flat plate, as is the case for the shock tube boundary layer, is nonstationary.

The nonstationary laminar boundary layer equations for a partially ionized gas have been treated by many authors and may be written as follows (Ref. 6)

$$\frac{\partial p}{\partial t} + \frac{\partial}{\partial x} (\rho u) + \frac{\partial}{\partial y} (\rho v) = 0 \quad (2.2.1)$$

$$\rho \left( \frac{\partial u}{\partial t} + u \frac{\partial u}{\partial x} + v \frac{\partial u}{\partial y} \right) = \rho \frac{\partial u_s}{\partial t} - \frac{\partial p_2}{\partial x} + \frac{\partial}{\partial y} \left( \mu \frac{\partial u}{\partial y} \right) \quad (2.2.2)$$

$$\frac{\partial p}{\partial y} = 0 \quad (2.2.3)$$

$$\rho \left( \frac{\partial H}{\partial t} + u \frac{\partial H}{\partial x} + v \frac{\partial H}{\partial y} \right) - \frac{\partial p_2}{\partial t} - u \frac{\partial p_2}{\partial x} - \frac{\partial}{\partial y} \left[ - q_c - q_d + \mu \frac{\partial}{\partial y} \left( \frac{u^2}{2} \right) \right] \quad (2.2.4)$$

where

$$q_c = -K \frac{\partial T}{\partial y}, \text{ the conductive heat flux}$$

and

$$q_d = -\rho D_A (e_I + 5/2 RT) \frac{\partial x}{\partial y}, \text{ the diffusive energy flux, assuming ambipolar diffusion.}$$

Equations (2.2.1-2.2.4) are respectively the continuity, x and y momentum and energy equations.

These equations may be reduced to steady state equations ( $\partial/\partial t = 0$ ) by a transformation of the co-ordinate system and changing the boundary conditions, as shown in Fig. 2. Equation 2.2.3 is a statement of the fact that the pressure is invariant through the boundary layer, (terms of the second order being neglected). If we assume that the freestream pressure is independent of x, then the steady-state equations are

$$\frac{\partial}{\partial x} (\rho u) + \frac{\partial}{\partial y} (\rho v) = 0 \quad (2.2.5)$$

$$\rho u \frac{\partial u}{\partial x} + \rho v \frac{\partial u}{\partial y} = \frac{\partial}{\partial y} \left( \mu \frac{\partial u}{\partial y} \right) \quad (2.2.6)$$

$$\rho u \frac{\partial H}{\partial x} + \rho v \frac{\partial H}{\partial y} = \frac{\partial}{\partial y} \left[ - q_c - q_d + \mu \frac{\partial}{\partial y} \left( \frac{u^2}{2} \right) \right] \quad (2.2.7)$$

If the gas remains in thermochemical equilibrium, the Saha equation (Eq. A1) can be used to directly relate the degree of ionization  $\alpha$  to temperature  $T$ , for a given pressure. In this case the energy equation (Eq. 2.2.7) may be reduced to the familiar classical form (Ref. 14)

$$\rho u \frac{\partial H}{\partial x} + \rho v \frac{\partial H}{\partial y} = \frac{\partial}{\partial y} \left( \frac{\mu}{Pr} \frac{\partial H}{\partial y} \right) + \frac{\partial}{\partial y} \left[ \mu \left( 1 - \frac{1}{Pr} \right) \frac{\partial}{\partial y} \left( \frac{u^2}{2} \right) \right] \quad (2.2.8)$$

provided that the Prandtl number,  $Pr$  relating viscosity and heat conduction, is defined as

$$Pr = \frac{\mu C_p}{K_{TOT}}$$

Models for the transport properties are developed in Appendix A. Using the results obtained there we have

$$\mu = \frac{5\pi}{32} \frac{m_A U_A}{Q_{AA}} \frac{1 + \frac{\alpha}{1-\alpha} \frac{Q_{AI}}{Q_{AA}}}{\frac{1 + \frac{\alpha}{1-\alpha} \frac{Q_{AI}/Q_{AA} + \alpha/1-\alpha}{Q_{AA}}}{1 + \frac{\alpha}{1-\alpha} \frac{Q_{AI}}{Q_{AA}}}} \frac{Q_{II}}{Q_{AA}} \quad (2.2.9)$$

$$C_p = R \left[ \frac{5}{2} (1+\alpha) + \frac{5}{2} T \left( \frac{\partial \alpha}{\partial T} \right)_p + e_I \left( \frac{\partial \alpha}{\partial T} \right)_p \right] \quad (2.2.10)$$

$$K_{TOT} = K + \alpha \frac{(1-\alpha)}{2} D_A \frac{P}{R} \left[ \frac{5}{2} + \frac{e_I}{T} \right]^2 \quad (2.2.11)$$

Note that the definition of the total thermal conductivity  $K_{TOT}$  includes the normal thermal conductivity  $K$ , as well as a diffusive energy transport term.

In classical boundary layer theory,  $Pr$  is generally assigned a constant value since it is virtually independent of temperature at the usual temperatures considered. However, in the case of ionized boundary layers the range of temperature from the cold wall to the hot freestream is so great that variations in viscosity, specific heat and thermal conductivity are such as to cause significant changes in  $Pr$ .

If the assumption of thermochemical equilibrium is not made, another formulation of the energy equation may be obtained (Ref. 6) i.e.,

$$\rho u \frac{\partial H}{\partial x} + \rho v \frac{\partial H}{\partial y} = \frac{\partial}{\partial y} \left( \frac{\mu}{Pr} \frac{\partial H}{\partial y} \right) + \frac{\partial}{\partial y} \left[ \mu \left( 1 - \frac{1}{Pr} \right) \frac{\partial}{\partial y} \left( \frac{u^2}{2} \right) \right] + \frac{\partial}{\partial y} \left[ \frac{\mu}{Pr} (Le-1) h_I \frac{\partial \alpha}{\partial y} \right] \quad (2.2.12)$$

where  $\text{Pr}'$  is based on values of  $C_p'$  and  $K'$  defined as

$$C_p' = 5/2 R (1 + \alpha) \quad (2.2.13)$$

$$K' = K \quad (2.2.14)$$

In Eq. 2.2.12, the Lewis number is defined as

$$\text{Le} = \frac{\rho D_A \text{Pr}'}{\mu} \quad (2.2.15)$$

where  $D_A$  is the ambipolar diffusion coefficient. The ratio of Prandtl number to Lewis number is referred to as the Schmidt number,  $\text{Sc}$

i.e.,

$$\text{Sc} = \frac{\text{Pr}'}{\text{Le}} = \frac{\mu}{\rho D_A} \quad (2.2.16)$$

In addition to the extra term which appears in the energy equation, an equation for species conservation must be solved. For ions, this is

$$\rho u \frac{\partial \alpha}{\partial x} + \rho v \frac{\partial \alpha}{\partial y} = \frac{\partial}{\partial y} \left( \rho D_A \frac{\partial \alpha}{\partial y} \right) + \dot{w} \quad (2.2.17)$$

assuming ambipolar diffusion, where  $\dot{w}$  is the species net production rate. For equilibrium flow, of course, Eq. 2.2.17 may be replaced by the Saha equilibrium composition relation (Eq. A.1). However, for nonequilibrium solutions, Eq. 2.2.17 must be considered along with the energy equation 2.2.12.

The theoretical results presented for the freestream relaxation region were obtained by Liu, based on an extension of the analysis presented in Sec. 2.1. A full description of this is presented in Ref. 15.

The theoretical equilibrium boundary layer results given in this report were obtained by Whitten (Ref. 16), while a complete boundary layer analysis for equilibrium, frozen and nonequilibrium flow is presented in Ref. 15.

### 3. DESCRIPTION OF EXPERIMENTAL EQUIPMENT AND TECHNIQUES

Since the original construction of the UTIAS 4" x 7" hypervelocity shock tube, several improvements have been made to the facility, increasing both its performance and capability to the level required for the successful outcome of the experimental program described in this report. These modifications concern the driven section vacuum system and the electronic timing circuits associated with shock speed measurement and triggering of the optical system's light source. Figure 3 illustrates the test section end of the facility.

#### 3.1 The Shock Tube

The design and construction of the UTIAS 4" x 7" shock tube is described

in Ref. 17.

A combustion driver using a stoichiometric mixture of 7.5% (by pressure) oxygen, 20% hydrogen and 72.5% helium, was used to create, by combustion, the required driver pressure  $P_4$ . This mixture was determined by Bristow (Ref. 18) to give a smooth combustion and an acceptable rise time and peak pressure. The gas mixture was ignited impulsively by means of a tungsten wire (0.015" dia.) located down the centre of the driver and across which a 13 KV potential was applied.

The ratio of combustion pressure  $P_4$  to test gas pressure  $P_1$  was found by Bristow to be related to the incident shock wave Mach number by the empirical expression,  $\ln(P_4/P_1) = [0.422 M_s^5 + 4.02]$  in the range  $10 \leq M_s \leq 24$ . The factor by which the stoichiometric gas mixture pressure,  $P_{MIX}$  is increased by combustion is approximately 6.7.

Design of the diaphragms was an important factor in the series of experiments conducted here since repetition of flow conditions was required in order that the boundary layer could be studied at different stations behind a shock wave of given strength. Accurate prediction of the shock speed was also important, as will be seen later, in triggering the light source for the optical equipment.

The diaphragms, made from type 304 stainless steel and annealed, were scribed to ensure proper petaling when burst. Following Bristow, whose calibration of this type of diaphragm is given in Ref. 18, the bursting pressure  $P_4$  is related to the diaphragm thickness  $t$ , the thickness after scribing  $h$ , the unsupported diameter  $d$  and the ultimate tensile strength of the material  $\sigma$ , by the equation

$$P_4 = \left( \frac{4\sigma t}{d} \right) K \left( \frac{h}{t} \right)^n$$

where  $K$  is a factor close to unity, depending on  $t$  and  $n$  is an experimentally determined value ( $\approx 2.2$ ). (see Ref. 18 for specific values of  $K$ ).

The driven section of the tube is 48 ft in length, the test section being located approximately 45 ft from the diaphragm station. The material used for construction of the driven section was a high strength alloy steel (type SPS-245) with the internal surfaces being ground to a 32 micro-inch finish and plated with a 0.002 inch layer of chromium.

Between experiments the tube was blown out with high pressure air and cleaned with acetone and trichlorethylene so as to maintain a reasonable degree of cleanliness.

The vacuum pump system for the driven section of the tube consists of a Kinney type KS-47 mechanical pump, a Heraeus Roots type VP-RG-350A pump and a CVC type PMCS-6B diffusion pump which in series were capable of bringing the tube pressure down to  $10^{-6}$  mmHg, with an outgassing rate of about  $1 \times 10^{-7}$  mmHg/min. Generally, the tube was pumped down for 3 to 4 days between experiments to ensure as good a vacuum as possible.

The argon test gas (with a purity of 99.996% by volume) was introduced directly into the driven section immediately before an experiment was carried out,

and the pressure monitored by a Wallace-Tiernan gauge (0-50 mmHg range). In each experiment a test gas initial pressure of 5 mmHg was set by this gauge. A more accurate measurement of the pressure was taken using an oil manometer, isolated before the experiment was conducted. This instrument is described in Ref. 18, along with its calibration.

For the one experiment in which it was required to add a small percentage (0.4% by pressure) of hydrogen to the test gas, a reservoir of known volume was required. The following procedure was adopted. Using the known volumes of the dump tank (35.4 ft<sup>3</sup>) a volume  $V_2$  is calculated as 45.0 ft<sup>3</sup>. With an arbitrarily set pressure of 40 mmHg ( $P_1$ ) in the hydrogen gas line (as measured by a Wallace & Tiernan gauge), the hydrogen was released into the tube and the pressure ( $P_2$ ) measured with a Mcleod gauge.

Using the standard equation,  $P_1 V_1 = P_2 V_2$ , the volume ( $V_1$ ) of the hydrogen gas line (including pressure gauge volume) was calculated.

### 3.2 Shock Velocity Measurement

Measurements of shock velocity were obtained between a reference station and 4 positions in the tube using standard piezoelectric pressure transducers, whose outputs were amplified before being applied to 2 Hewlett-Packard (type 3734 A) and 2 Racal electronic counters (see Fig. 4), measuring in micro-second units. A fifth velocity measurement was taken across two feet of the test section using a Hewlett-Packard (type 5325 A) counter measuring in 0.1 micro-second units.

As mentioned in Ref. 18, the degree of shock attenuation recorded with this system is so low as to lie within the experimental error of the velocity measurement technique.

A Kistler pressure transducer was used (station G, Fig. 4) to record an oscillogram of the pressure history through the shock wave and subsequent gas flow.

### 3.3 Optics

The optical system employed in this experimental program comprised a pulsed dual-frequency laser, a Mach-Zehnder interferometer and a plate camera. Figure 5 shows a schematic layout of the optics and Fig. 6 gives a plan view of the experimental apparatus.

#### 3.3.1 Light Source

A TRG 104A ruby laser, pulsed by a Pockels cell Q-switch and fitted with a second harmonic generator, provided the 6943 Å and 3471.5 Å component wavelength light source. A full description of this laser and its advantages and disadvantages over more conventional light sources is given in Ref. 18. The ruby rod of this type of laser is energized by a flash-lamp for a period of about 950 usecs before the optimum condition is obtained, prior to Q-switching. A signal from one of the aforementioned pressure transducers is used, via a delay unit, to trigger the flash lamp and a similar signal from another transducer is used, again via a delay circuit, to trigger the Pockels cell at a predetermined time (see Fig. 4). In this manner the desired region of flow is exposed to the film plates. This system of shuttering releases a short burst of light in the order of 20 nanoseconds, which is instantaneous relative to the shock speed (say 5 Km/sec). Of

course accurate knowledge of the shock speed is required prior to a run for successful operation of the laser-shutter system. A measurement of the time elapsed between the shock-wave arrival at a reference station and operation of the Q-switch is recorded on a Hewlett-Packard (type 3734 A) counter (see Fig. 4) and this, in conjunction with a shock speed measurement from the same reference, enables an accurate determination of the flow field exposed to the plates, with respect to the shock wave. This is essential for cases where the shock wave is outside the field of view.

A short focal length (150 mm) convex lens, whose selection is determined by the maximum focal length that will achieve the necessary collimation of light to the required field, is used to focus the laser beam onto a light diffuser placed at the focal point of the first parabolic mirror of the interferometer. The introduction of a diffuser reduces the spatial coherence of the laser light, resulting in better quality interferograms.

### 3.3.2 Mach-Zehnder Interferometer

The design and construction of the Mach-Zehnder interferometer used in these experiments is described in Ref. 19. The adjustment procedure for obtaining the required fringe system is described in that report. The alignment procedure for this study, involving the interferometer and the light source, is described in detail in Appendix B.

### 3.3.3 Interferogram Photography

The camera used for the photography is shown schematically in Fig. 5. It consists of a shutter (nontriggerable), a beam splitter (60%-40%), a plane mirror and 2 line filters to separate out the component wavelengths. It is designed to hold 4" x 5" film plates.

Two lenses were used to obtain the required overall magnification ( $\approx 1.8$ ). A schematic ray diagram of this arrangement is shown in Fig. 7. Apart from the magnification factor, the lens selection was made with several other criteria in mind. These may be summarized as follows:

- i) The combination of the focal lengths of the lenses chosen to give the desired magnification must be compatible with the physical limitations of the camera and space between the camera and interferometer.
- ii) The aperture of the light beam at any station must fall within the bounds of the lens, filter, splitter and mirror apertures. Working at the outer edges of lenses can give rise to fringe distortions and focussing problems.
- iii) The beam must not be focussed in the plane of any of the optical elements, since burning of the element may occur.
- iv) The use of an ultra-violet light source (as is the 3471.5 Å) poses some problems since this wavelength falls at the lower end of the bandwidth for which glass lenses are useful. The transmission of light is poor and the thicker the lens, the more the light lost.
- v) The overall magnification also determines the intensity of light available to the film. The use of a second harmonic generator cuts down on the available light energy from the laser and while there is no problem with the

primary ( $6943 \text{ \AA}$ ) wavelength, the secondary ( $3471.5 \text{ \AA}$ ) wavelength requires that the laser be very finely tuned.

Figure 8 illustrates the advantage of using as large a magnification as possible for the film plate, rather than relying completely on enlarging when printing.

The film used for the experiments was Kodak Royal X Pan (1250 ASA) in 4" x 5" plates. Different developers were tried (DK-50, D-11, D-8) to improve the fringe definition on the negatives. It was found that a undiluted DK-50 solution gave the best results with a developing time 20% longer than that recommended.

Enlargements of between 6 and 8 times the negative size were printed, giving an overall magnification of 12 to 16 over the laboratory scale. Kodak type 1594 grade 4 industrial paper (in rolls of 40" x 100') was used for this purpose. Limits on the size of prints made, were imposed mainly by the practical aspects of developing and general ease of handling in the darkroom.

### 3.3.4 Test Section Plane of Focus

The problem of fixing a plane of focus in the test section and also that of providing a suitably accurate scale on the interferograms was overcome in the following manner.

Several holes were drilled in a metal plate at approximately 1 cm intervals. Cross-hairs were placed over each of these holes and the distances between cross-hairs measured accurately with a Hilger T.500 Universal Measuring Projector (accurate to 0.00001"). This plate was fixed in the interferometer between the second mirror and second splitter (see Fig. 9), making sure that the plane of the cross-hairs was perpendicular to the light beam. The optimum plane of focus in the test section is a matter of conjecture. Following Ref. 20, where it is shown that refraction errors are minimized by focussing on a plane 2/3 across the test section from the window nearest to the light source, the cross-hairs were first fixed in the test section and an image focus plane position established (using only the parabolic mirror,  $P_2$ ) before being moved into the compensating chamber light beam path and adjusted in position until they were again brought into focus.

The cross-hairs served another useful purpose in that of determining the true position of the shock tube wall. As can be seen from the flow interferograms, (e.g., Figs. 11, 12 and 13) the real wall surface is ill-defined owing to the effects of refraction of the light through the boundary layer density gradient. Before each experiment the camera was focussed on the wall edge nearest the camera (which gave the clearest wall image) and the fringes blanked out near the wall by means of a plate inserted in the compensating arm of the interferometer. A photograph was then taken (one for each wavelength) and used to measure the distances from the cross-hairs to the wall surface (Fig. 10). These distances (when adjusted by the correct magnification factor) were used to determine a wall position on the interferograms (with an estimated accuracy of  $\pm 0.05 \text{ mm}$ ), which as can be seen in Appendix C, is important in the analysis of the interferograms.

This method of using corresponding planes in the test section and compensating arms of the interferometer is felt to be very useful for experiments in which it is desired that no obstruction be placed in the shock tube that may disturb the flow.

## 4. RESULTS AND DISCUSSION

### 4.1 Shock Front

Measurements of fringe shift through the Rankine-Hugoniot shock front were taken from the interferograms of three experiments, i)  $M_s = 16.53$  (pure argon), ii)  $M_s = 16.68$  (argon + 0.4%  $H_2$ ) and iii)  $M_s = 13.59$  (pure argon). The interferograms are shown in Figs. 11, 12 and 13 respectively. The Rankine-Hugoniot front is visible, on the right-hand side of the interferograms, as an almost discontinuous shift in the fringes. The shift through this front for  $\lambda_2$  (about 1.5 for the conditions described here) is theoretically twice that for  $\lambda_1$  assuming frozen flow conditions immediately behind the front (i.e.,  $\alpha = 0$ ). Due to the very high density gradient through the front, it appears considerably thicker than is really the case. This will be discussed in more detail later. The measurements of fringe shift (i.e., the displacement of a fringe between the undisturbed gas region and a reasonably uniform flow region behind the front) were substituted into the interferometric equations (Eqs. C10 and C11) and  $\rho$  and  $\alpha$  calculated as shown in Table I.

TABLE I: EXPERIMENTAL DATA

$M_s$	$P_1$ (mmHg)	$S\lambda_1$	$S\lambda_2$	$\rho$ ( $\text{kg/m}^3$ )	$\alpha$ (%)	$\rho_{th}$ ( $\text{kg/m}^3$ )	$\alpha_{th}$ (%)
16.53	5.12	0.724	1.520	$4.314 \times 10^{-2}$	$-6.74 \times 10^{-2}$	$4.380 \times 10^{-2}$	0.0
16.68	5.17	0.715	1.599	$4.558 \times 10^{-2}$	$3.52 \times 10^{-1}$	$4.412 \times 10^{-2}$	0.0
13.59	5.09	0.744	1.608	$4.525 \times 10^{-2}$	$2.03 \times 10^{-1}$	$4.328 \times 10^{-2}$	0.0

Agreement with the theoretical density values  $\rho_{th}$ , as predicted by the Rankine-Hugoniot relations, is reasonably good although more so for the stronger shock cases. Verification of the frozen nature of the gas behind the shock front is given by the negligible degree of ionization.

An estimate of the error involved with these  $\rho$  and  $\alpha$  calculations may be determined using the classical error equation derived in Ref. 21.

$$Q = \left\{ \frac{\partial f}{\partial a_1} \right\}^2 q_1^2 + \left\{ \frac{\partial f}{\partial a_2} \right\}^2 q_2^2 + \left\{ \frac{\partial f}{\partial a_3} \right\}^2 q_3^2 + \dots \quad (4.1.1)$$

where  $Q$  is the error in the calculated quantity  $A$ , which is a function of the measured quantities  $a_1, a_2, a_3$  etc. [i.e.,  $A = f(a_1, a_2, a_3 \dots)$ ] and  $q_1, q_2, q_3$  etc., are the errors in  $a_1, a_2, a_3$  etc.

This equation may be applied to the interferometric equations, Eqs. (C10) and (C11), as described in Ref. 22. For nondimensional fringe shift measurement errors of 0.03, the errors predicted by Eq. 4.1.1 in density  $\rho$  and degree of ionization  $\alpha$  are respectively  $9.53 \times 10^{-4}$   $\text{kg/m}^3$  (or 2.1% of the predicted frozen value,  $\rho_2$ ) and 0.21%.

As mentioned earlier, the apparent shock front thickness (approximately

1.5 mm) is considerably greater than the theoretical value. From Ref. 23 the limiting value for shock front thickness ( $M_s \rightarrow \infty$ ) is  $1.42 l_0$ , where  $l_0$  is the mean free path length of the undisturbed gas. For the conditions  $P_1 = 5$  torr and  $T_1 = 300^\circ\text{K}$ ,  $l_0 = 2 \times 10^{-4}$  inches for argon, which gives a limiting shock front thickness of  $2.84 \times 10^{-4}$  inches. Thus there is a great difference between the observed shock front thickness and the theoretically predicted value. This may be explained by a combination of errors. Firstly, considering refraction, the density gradient through the front is large (typically  $4.5 \text{ Kg/m}^3/\text{m}$  for a linear gradient). However if we assume that the interferometer is perfectly aligned (normal to the test section) any light ray passing through the shock front will be refracted very quickly out of the thin front region into the uniform region behind it. Consequently errors due to refraction may be ignored for the perfectly aligned interferometer. However, if the interferometer is misaligned, even to a small degree, then refraction effects become quite significant, since many more rays pass through the front.

The alignment procedure described in Appendix B is not as accurate about the y-axis as it is about the x-axis of the shock tube because there is no reference surface available on which to observe the spurious fringes associated with misalignment. Consequently, a two-dimensional effect is inevitable when looking at the thin shock front region.

The fact that the shock front appears considerably thicker for the weaker shock may be the result of poorer alignment and consequently a larger two-dimensional effect. The interferometer and the light source were left undisturbed as far as possible. However, a major adjustment of the interferometer was made prior to the weaker shock experiment and it is reasonable to suppose that a poorer alignment was achieved about the y-axis. This would also account for the somewhat larger discrepancy between calculated and predicted frozen density values behind the weaker shock front.

#### 4.2 Freestream Relaxation Region

The interferograms shown in Fig. 11 illustrate well the structure of an ionizing shock wave. As discussed in the previous section, the Rankine-Hugoniot front is evident as a sudden, almost discontinuous shift in the fringes. Behind this front, changes in the flow properties take place slowly as the gas begins to relax (this shows up as a region in which fringe changes are virtually indiscernible). The 'ionization front', through which a rapid increase in the degree of ionization takes place up to equilibrium value, is apparent as a closing together of the fringes.

It may be noted that while a nondimensional fringe shift through the Rankine-Hugoniot front is about 0.75 for  $\lambda_1$  and 1.5 for  $\lambda_2$  for a density ratio of about 4, the shifts through the 'ionization front' are larger (5.5 for  $\lambda_1$ , and 2 for  $\lambda_2$ ) even though the density ratio is only about 2. This may be accounted for by the negative electron contribution to refractive index, to which the higher wavelength is more sensitive.

Analysis of the interferograms illustrated in Figs. 11-13 together with those of Fig. 14, with the method described in Appendix C, yield the freestream relaxation region density and ionization profiles given in Figs. 15 and 16. The values  $\rho_1$ ,  $\rho_2$  and  $\rho_3$  are respectively the initial pre-shock gas density, the frozen (Rankine-Hugoniot) density and the post-relaxation equilibrium density. The limit of  $\rho_2/\rho_1$  in the perfect gas case is 4 [i.e.,  $P_2/P_1 \rightarrow \infty$ ,  $\rho_2/\rho_1 \rightarrow (\gamma_1+1)/(\gamma_1-1)$ , where

$\gamma$  is the specific heat ratio,  $\gamma = 5/3$ ], for a monatomic gas. From Fig. 15, the density ratio  $\rho_2/\rho_1 = 3.96$  for a pressure ratio of  $P_2/P_1 = 345$  across the shock front, while from Fig. 16,  $\rho_2/\rho_1 = 3.94$  for  $P_2/P_1 = 231$ . The real (imperfect) gas density ratio  $\rho_3/\rho_1$ , which relates equilibrium gas density to that of the pre-shock state, has values of  $\rho_3/\rho_1 = 7.74$  for  $P_2/P_1 = 398$  (argon) and  $\rho_3/\rho_1 = 7.83$  for  $P_2/P_1 = 405$  (argon + hydrogen) from Fig. 15, and from Fig. 16,  $\rho_3/\rho_1 = 6.08$  for  $P_2/P_1 = 258$ .

A comparison between initial, frozen and equilibrium flow properties for pure argon is made in Table II.

TABLE III: SHOCK WAVE FLOW PROPERTIES

$M_s = 16.53$						
	P(torr)	$\rho(\text{kg/m}^3)$	T( $^\circ\text{K}$ )	$u(\text{m/s})$	$\alpha(\%)$	$n_e(\text{/m}^3)$
Initial (1)	5.12	0.0111	297	0	0	0
Frozen (2)	1749	0.0438	25,588	3962	0	0
Equilibrium (3)	2038	0.0857	13,158	4618	15.78	$2.039 \times 10^{23}$
$M_s = 13.59$						
	P(torr)	$\rho(\text{kg/m}^3)$	T( $^\circ\text{K}$ )	$u(\text{m/s})$	$\alpha(\%)$	$n_e(\text{/m}^3)$
Initial (1)	5.09	0.0110	297	0	0	0
Frozen (2)	1175	0.0433	17,390	3253	0	0
Equilibrium (3)	1315	0.0668	11,741	3643	7.42	$7.47 \times 10^{22}$

Figure 15 indicates that the relaxation length for a shock wave of Mach number 16.53 travelling into pure argon ( $P_1 = 5.12$  torr) is about 2 cms. This is rather longer than the theoretical value predicted by Hoffert and Lien (Ref. 1) who, for the conditions  $M = 16.5$  and  $P_1 = 5.0$  torr, give a relaxation length of 1.6 cms. The experimental results obtained by Wong and Bershadar (Ref. 3) give a value of 1.22 cms. for corresponding conditions. The effects of radiation losses in the post shock-wave equilibrium region are evident in the gradual decrease in  $\alpha$  and  $\rho$ .

The results for relaxation behind a shock of Mach number  $M_s = 13.55$  moving into argon ( $P_1 = 5.09$  torr) are shown in Fig. 16. A relaxation length of approximately 8.0 cm<sup>2</sup> is obtained which compares favourably with Hoffert and Lien's predicted value of 7.6 cm. for corresponding conditions. Wong and Bershadar give a result of 6.1 cms which again is somewhat lower. The experimental equilibrium value of ionization of about 4.5% is considerably lower than the predicted value of 7.5%. There is also a good deal of scatter in the experimental results, notably density. The usefulness of the interferometric experimental technique must be questioned in flow regions where density and degree of ionization changes are very small and the resulting fringe shifts and refractive index changes

are of the same order as the errors associated with such measurements.

Applying the error equation given in Sec. 4.1 (Eq. 4.1.1) to the interferometric equations, Eqs. (C6) and (C7) the respective errors for  $\rho$  and  $\alpha$  are  $0.5 \cdot 10^{-4}$  Kg/m<sup>3</sup> (or 2% of  $\rho_2$ ) and 0.1%, for a refractive index difference ( $N$ ) error of  $10^{-7}$ . From the theoretical profiles shown in Fig. 16 the average change in  $\rho$  and  $\alpha$  over the first 5 cms. may be taken as  $0.0002$  Kg/m<sup>3</sup>/cm (or 0.5% of  $\rho_2$  per cm) and 0.1%/cm. respectively. For an interferogram with fringes spaced by 2.0 mm the change in  $\rho$  and  $\alpha$  from fringe to fringe expected is  $4 \cdot 10^{-5}$  Kg/m<sup>3</sup> (0.1% of  $\rho_2$ ) and 0.02%, which are considerably smaller quantities than the experimental error values. Consequently, the shorter the relaxation region (or the smaller the region of small flow changes) the better should be the agreement between experiment and theory (with less scatter in the experimental data). This is well illustrated by the three sets of results shown in Figs. 15 and 16, the best agreement being obtained with the argon + hydrogen data, which will now be discussed.

Bristow (Ref. 18) discussed the use of hydrogen addition with a view to eliminating some inexplicable flow disturbances both in and behind the shock wave. The same type of disturbances were observed at higher Mach numbers in this series of experiments. However since only a comparatively small aperture of the flow field was observed in each experiment, the disturbances were not so apparent. Figure 17 shows interferograms obtained by Bristow for an ionizing shock wave ( $M = 17$ ) over the complete 7 inch aperture of the shock tube. Some possible causes of these flow disturbances are suggested but not explained in Ref. 18. The addition of 0.4% H<sub>2</sub> (by pressure) to the argon test gas was found by Bristow to eliminate these disturbances. The effect of hydrogen impurity on the shock wave relaxation length is quite drastic (Fig. 12). A comparison with the pure argon gas case is made in Fig. 15, where it is seen that the relaxation length is reduced from 20 mm to approximately 6 mm, for similar conditions. This may be explained by the larger excitation collision cross-sections for H-H and H-e as compared with those for A-A and A-e. A full discussion on the effect of hydrogen addition is given by Liu in Ref. 15.

It is worth noting that the equilibrium degree of ionization is rather lower (13.5%) than that predicted for pure argon (16.31%) while density is higher (0.0975 Kg/m<sup>3</sup> as opposed to 0.0873 Kg/m<sup>3</sup> for pure argon). The major reason for this is the effect of the low hydrogen atomic mass (about 1/40 of that for argon), as described in Ref. 15.

The theoretical results obtained by Liu show good agreement with experiment both for the pure gas case and with hydrogen additive.

#### 4.3 Wall Effects in Relaxation Region

Perhaps the most interesting results obtained in this experimental program were obtained in the relaxation region close to the shock tube wall (see Figs. 11-14). These are believed to be the first of such experimental data obtained in this region.

A large concentration of electrons is apparent as a sheath growing from the shock front, the degree of ionization increasing much more rapidly than in the freestream. Figures 18 and 19 show contours of constant  $\alpha$  for shocks ( $M = 16.53$  and  $M = 13.59$ ) moving into pure argon. While similar effects are seen in both instances, the phenomenon is much more in evidence with the stronger shock as would be expected, the relaxation length being much shorter and the equilibrium degree of

ionization being about twice that for the weaker shock. It is difficult to conclude from the interferograms (Fig.12) whether a similar wall effect occurs with the addition of hydrogen to argon test gas. The relaxation region was shortened to the extent that only a few fringes transmit data in the wall relaxation region. The fringe spacing should be reduced considerably from that shown in Fig. 12 (1.24 mm for  $\lambda_1$ , 1.10 mm for  $\lambda_2$ ) in order to obtain the required information.

The reasons for this premature ionization close to the wall are far from clear. One considered possibility was that a gas-surface interaction occurred between the argon plasma and the chromium plated steel shock tube wall. Two experiments were carried out to try and eliminate this possibility. In one, a covering (0.003") of ordinary Sellopac (cellophane) tape was stuck to the wall and in the other a thin tungsten foil (0.001") was fixed to the wall. It was hoped that the tape, being a good electrical insulator, or the tungsten, having a different work function than chromium or steel, might change the electron distribution if indeed a gas-surface interaction was taking place. However, no changes were apparent. Figure 20 shows interferograms of the shock wave passing over the tungsten foil. A weak Mach wave may be seen emanating from the leading edge of the foil at the left side of the interferogram.

The possibility of impurities being present on the shock tube wall must also be considered. The wall was cleaned as thoroughly as possible before each experiment. However the presence of water vapour molecules, typically at a density of  $10^{14}$  cm<sup>-2</sup> at a pressure of  $10^{-6}$  torr, must be considered a likely cause, since at the temperatures behind the shock front (say 20,000°K) any water vapour molecules would be completely dissociated and hydrogen, as already proven, has a dramatic effect on the ionization rates. However it is not clear how their presence would be felt in the freestream.

It is of interest to note that in another experimental study, in the same facility, involving the use of a finite flat plate model, a similar phenomenon was evident (Ref. 16).

#### 4.4 Boundary Layer

Before any experiments were conducted to obtain boundary layer data for ionized argon gas flows, a check on the experimental technique was made by obtaining some data for boundary layers behind weaker, nonionizing shock waves, that could be compared with well-established classical theory.

Figure 21 shows experimental data and a theoretical density profile at 10.0 cms behind a shock wave of Mach number  $M_s = 6.48$  travelling into argon test gas at initial pressure  $P_1 = 5.06$  mmHg. The experimental results agree reasonably well with the similarity solution obtained by Whitten (Ref. 16).

The errors involved in these data concern the shock tube wall location and fringe-shift measurements. Determination of the wall position, as described in Sec. 3.3.4, is subject to a  $\pm 0.05$  mm error. Following the error analysis described in Sec. 4.1, the resulting error in density calculations from fringe shift measurement errors of 0.03 in  $\Delta p = \pm 6.6 \cdot 10^{-4}$  Kg/m<sup>3</sup>, or  $\Delta p = 1.6\%$  of  $p_\infty$ , the freestream density value. Thus the largest source of error is the wall location error. This is represented in Fig. 21 by an error bar.

Figures 22 and 23 are flow and no-flow interferograms for  $\lambda_1$  and  $\lambda_2$  respectively, taken for a shock Mach number of 16.50 and  $P_1 = 5.63$  torr. The flow

disturbances mentioned in Sec. 4.2 are very much in evidence. Care was taken, when analyzing the boundary layer, to avoid regions in which disturbances were apparent. Figure 24 shows another set of flow interferograms capturing the boundary layer immediately behind a shock wave of similar strength ( $M_s = 16.47$ ,  $P_1 = 5.22$  torr).

Density and degree of ionization data taken at 3.75 cms behind the shock front are presented in Fig. 25, together with the equilibrium, frozen and non-equilibrium solutions obtained by Liu and Whitten. Details of their theoretical solutions are given in Refs. 15 and 16. The experimentally determined boundary layer thickness (based on a 99% density ratio value) is 0.7 mm while that predicted by equilibrium theory is 0.9 mm. Comparison with the theoretical models suggests that the boundary layer is either frozen or in nonequilibrium, which is contrary to the assumptions made by most authors.

Apart from errors arising from refraction effects, which are not considered in this study, the errors in  $\rho$  and  $\alpha$  due to wall position error became quite significant in dual-wavelength interferometry (Appendix C), maximizing towards the wall. Even for an error of only 0.05 mm in wall position, the resulting fringe shift error may be 0.3 close to the wall giving density and degree of ionization errors of 0.01  $\text{Kg/m}^3$  and 0.5% respectively or 10.7% and 3.2% of their respective freestream values.

Even though refraction errors have been neglected, the results of Kuiper (Ref. 24), for fringe shift error due to refraction through the end wall boundary layer, suggests that even close to the wall (0.2 mm) where refraction effects are strongest, the theoretical error is only 0.02 (for similar gas conditions), which is small compared to the fringe shift error due to wall position error.

Figure 26 shows flow interferograms of the boundary layer region between 18 and 24 cm behind a shock of Mach number 16.49. It may be appreciated from a qualitative study of the interferograms, that the boundary layer thickens considerably in this region (to the left). Measurements indicate that at  $x_s = 20.0$  cm, the boundary layer is approximately 2mm, while at  $x_s = 22.5$  cm it has thickened to about 4 mm. In the absence of any thin-film gauge traces, it might be inferred from this rapid thickening of the boundary layer, that transition from laminar to turbulent flow is taking place.

For a Reynold's number defined as (Ref. 11)

$$Re = \frac{V_2 \times \rho_e}{\mu_e} \left[ 1 - \frac{V_1}{V_2} \right]^2$$

where  $V_2 = u_s - u_2$ ,  $V_1 = u_s$ , a Reynold's number of  $Re = 2.65 \times 10^6$  is obtained.

Experimental and theoretical profiles for  $x_s = 20.0$  cms are shown in Fig. 27 and again the large differences between equilibrium theory and experiment may be noted.

Additional errors to those mentioned earlier may arise in this case due to the fact that since the shock wave is not in the field of view, the exact determination of  $x_s$  is not possible. However from recorded time measurements, i.e., the times between the shock wave passing through the centre of the test section and the time at which the Pockels cell is triggered, the position of the shock wave

with respect to the field of view may be determined to within  $\pm 0.5$  cms or better. The errors incurred in  $\rho$  and  $\alpha$  are virtually negligible.

Figure 28 shows results taken 12 cms. behind a shock wave of  $M = 13.56$ , where the experimental density boundary layer thickness is about 1.2 mm while a boundary layer thickness based upon a degree of ionization ratio  $\alpha/\alpha_e = 0.99$  appears to be significantly greater at approximately 1.6 mm. This suggests the presence of a thermal boundary layer which is rather thicker than the viscous boundary layer.

## 5. CONCLUSIONS

The use of dual-wavelength interferometry has proven successful in the study of ionizing shock-wave structure and the shock-tube boundary layer in argon.

Results taken of the shock front thickness indicate that the interferometer-light source alignment procedure, described in Appendix B, should be extended to improve alignment about the y-axis of the shock tube.

Although the effects of refraction through the shock front are considered to be slight for a perfectly aligned interferometer, a full analysis should be carried out to determine the magnitude of refraction errors for a misaligned interferometer.

The measurements of density and ionization in the relaxation region show good agreement with theory although the scatter in experimental results for weaker shocks ( $M \approx 13.5$ ) suggest that further work should be directed at stronger shock studies of that the laser ruby element (6943 Å) be replaced by a neodymium-glass element (10600 Å) for greater sensitivity to electron density for weaker shocks.

The contribution of excited state refractivities for neutral argon and the effect on  $\rho$  and  $\alpha$  calculations should be investigated for strong shocks (Ref. 16).

The phenomenon of a faster ionization rate taking place close to the wall was an unexpected result of this experimental investigation. A more detailed study of this should be carried out to establish whether the phenomenon is peculiar to the particularly larger-area shock tube used in this experimental program or whether it applies to shock tubes of smaller size, where this phenomenon has apparently not been noticed (e.g., Ref. 3).

The results obtained for the induced boundary layer, when compared with the equilibrium, frozen and nonequilibrium theoretical profiles of Liu and Whitten, suggest that the boundary layer is in a frozen or nonequilibrium state. The latter profiles are very similar and it is virtually impossible to distinguish between them experimentally.

Although the experimental results presented take no account of refraction effects in the boundary layer, the theoretical error results presented in Ref. 24 indicate that errors due to refraction are small compared to the wall location error.

The freestream conditions used in the calculations were those predicted by equilibrium strong-shock theory (Ref. 16). Any losses due to radiation in the freestream were neglected. Results presented in Ref. 25 for a shock of Mach number 16.3 and  $P_1 = 5$  torr, indicate that the degree of ionization drops from an equilibrium value of about 15% immediately behind the shock wave to 10% at 5 cm behind the shock,

after which it remains fairly constant. Corresponding changes in density are relatively small (typically 5% of the equilibrium value,  $\rho_2$ ). Reference 22 gives some data for radiation losses obtained in the facility used for this study, pertaining to stronger shocks.

Although tentative indications of transition in the boundary layer were present for the stronger shock case, in the form of a rapid growth, no definite proof was obtained. A further study of transition behind ionizing shocks should include the use of a thin-film heat-transfer gauge.

The shock-transition density and degree of ionization profiles as well as those through the boundary layer, together with similar contours of the rapid ionization region near the wall should provide useful data for additional theoretical research.

References

1. Hoffert, M. I.  
Lien, H.  
J. Phys. Fluids 10, 1769 (1967).
2. Enomoto, Y.  
J. Phys. Soc. Japan 35, 1228 (1973).
3. Wong, H.  
Bershader, D.  
J. Fluid Mech. 26, 459 (1966).
4. Nelson, H. F.  
J. Phys. Fluids 16, 2132, (1973).
5. Knöös, S.  
J. Plasma Physics, 2, 207 (1968).
6. Back, L.H.  
J. Phys. Fluids, 10, 807 (1967).
7. Ackroyd, J. A. D.  
Rept. 107, Dept. Mech's. Fluids. University of Manchester, (1968).
8. Macken, N. A.  
Besse, A. L.  
Levine, M. A.  
AIAA J. 10, 1129 (1972).
9. Burminskii, E. P.  
Goriachev, V. L.  
Sukhov, G. S.  
J.Tech. Physics. 38, 1482 (1968).
10. Kamimoto, G.  
Teshima, K.  
C.P. 32, Dept. Aero. Engr. University of Kyoto, Japan, (1972).
11. Glass, I.I.  
Hall, J. G.  
Handbook of Supersonic Aerodynamics. NAVORD Report No. 1488 (6), (1959).
12. Ya. B. Zel'dovich.  
Yu. P. Raizer.  
"Physics of Shock Waves and High-Temperature Hydrodynamic Phenomena", 2, Academic Press (1967).
13. Liepmann, H. W.  
Roshko, A.  
"Elements of Gasdynamics", John Wiley & Sons, Inc. (1957).
14. Stewartson, K.  
"The Theory of Laminar Boundary Layers in Compressible Fluids", Oxford Mathematical Monographs. (1964).
15. Liu, W. S.  
University of Toronto, Inst. for Aerospace Studies, Report No. (to be published).
16. Whitten, B. T.  
University of Toronto, Inst. for Aerospace Studies, Ph.D. Thesis (to be published).
17. Boyer, A. G.  
University of Toronto, Inst. for Aerospace Studies, Report No. 99 (1965).
18. Bristow, M.P.F.  
University of Toronto, Inst. for Aerospace Studies, Report No. 158 (1971).

19. Hall, J. G. University of Toronto, Inst. for Aerospace Studies,  
Report No.27, (1954).
20. Wachtell, G.P. "Refraction Error in Interferometry of Boundary Layer  
in Supersonic Flow Along a Flat Plate". Ph.D. Thesis,  
University of Princeton, (1951).
21. Tuttle, L.  
Satterly, J. "The Theory of Measurements". Longmans, Green & Co.,  
London (1925).
22. Igra, O. University of Toronto, Inst. for Aerospace Studies,  
Report No.161 (1970).
23. Sakurai, A. J. Fluid Mech. 3, 255 (1957).
24. Kuiper, R. A. "Interferometric Study of the Nonequilibrium Shock Re-  
flection Process and Thermal Layer in Ionizing Argon",  
SUDAAR Report No.353, Stanford Univ, (1968).
25. Oettinger, P. E. "A Unified Treatment of the Relaxation Phenomenon in  
Radiating Argon Plasma Flows Behind Incident and Bow  
Shock Waves", SUDAAR Report No. 285, Stanford Univ,  
(1966).

APPENDIX A: THERMODYNAMIC AND TRANSPORT PROPERTIES OF PARTIALLY IONIZED ARGON

One of the major difficulties in solving the boundary layer equations for an equilibrium partially ionized gas flow in the shock tube is the determination of the thermodynamic and transport properties (especially the latter) over the wide range of temperatures encountered through the boundary layer, from the cold (300 K) wall to the hot (typically 13,000 K) free-stream.

Some experimental data have been obtained (e.g., Ref. A1) in the shock tube, utilizing the hot slug of stagnant gas behind the reflected shock wave. However the majority of information provided in the literature is of a theoretical nature, sufficient to predict the thermal conductivity and viscous properties with a reasonable degree of accuracy.

Previous assumptions such as a constant Prandtl number and density-viscosity product are now known to be inaccurate.

The degree of ionization in equilibrium flow, for given pressure and temperature, is given by the Saha equation as

$$\alpha = \left[ 2.5 \frac{p}{T^{5/2}} e^{\frac{\theta_I}{T}} + 1 \right]^{-1/2} \quad (A1)$$

where  $p$  is in  $\text{N/m}^2$  and the characteristic temperature of ionization is  $\theta_I = 182,900^\circ\text{K}$ .

Following Ref. A2, enthalpy may be written as (neglecting excited state contributions)

$$h = R \left[ \frac{5}{2} (1 + \alpha) T + \alpha \theta_I \right] \quad (A2)$$

and the equilibrium specific heat at constant pressure,

$$c_p = \left. \frac{\partial h}{\partial T} \right|_p$$

as

$$c_p = R \left[ \frac{5}{2} (1 + \alpha) + \frac{5}{2} T \left( \frac{\partial \alpha}{\partial T} \right)_p + \theta_I \left( \frac{\partial \alpha}{\partial T} \right)_p \right] \quad (A3)$$

From (A1),

$$\left. \frac{\partial \alpha}{\partial T} \right|_p = 1.25 \alpha^3 p T^{-7/2} e^{\frac{\theta_I}{T}} \left( 2.5 + \frac{\theta_I}{T} \right) \quad (A4)$$

and substitution of (A4) into (A3) gives

$$C_p = R \left\{ \frac{5}{2} (1 + \alpha) + \left( \frac{5}{2} T + \theta_I \right) \left[ 1.25 \alpha^3 p T^{-7/2} e^{\theta_I/T} \left( 2.5 + \frac{\theta_I}{T} \right) \right] \right\} \quad (A5)$$

The collision cross-section data required for the calculation of viscosity and thermal conductivity may be summarized as follows:

i) Atom-atom collision cross-section  $Q_{AA}$  is

$$Q_{AA} = 17 \left( \frac{T}{10^4} \right)^{-0.26} \times 10^{-18} \text{ m}^2 \quad (A6)$$

from the curve fitted (Ref. A2) to the data provided by Ref. A3

ii) The Coulomb scattering cross-section,  $Q_{11}$  is (from Ref. A4)

$$Q_{11} = \frac{q^4}{4\pi\epsilon_0^2 (m_r v_r^2)^2} \ln \left[ \frac{4\pi\epsilon_0 m_r v_r^2}{q^2} \left( \frac{\epsilon_0 kT}{n_e q^2} \right)^{1/2} \right] \text{ m}^2 \quad (A7)$$

where  $m_r$  is the reduced mass (in this case  $m_A/2$ ),  $v_r$  is the random velocity given by

$$v_r = \left[ \frac{16}{\sqrt{\pi}} \left( \frac{kT}{m} \right)^{3/2} \right]^{1/3}$$

and  $n_e$  is electron number density,

i.e.,

$$n_e = \frac{\alpha}{1+\alpha} \frac{p}{kT}$$

$q$  is electron charge ( $1.6021 \times 10^{-19}$  Coulomb),  $\epsilon_0$  is permittivity of vacuum ( $8.854 \times 10^{-12}$  farad/m) and  $k$ , the Boltzmann constant ( $1.3804 \times 10^{-23}$  joule/ $^\circ\text{K}$ ). Substitution of the constants in Eq.(A7) yields

$$Q_{11} = \frac{7.47 \times 10^{-10}}{T^2} \ln \left[ 8.95 \times 10^6 \frac{T^{3/2}}{n_e^{1/2}} \right] \text{ m}^2 \quad (A8)$$

where the electron number density may be calculated from Eq. (A1).

iii) The atom-ion hard sphere collision cross-section is found to be virtually independent of temperature and a value of

$$Q_{Ai} = 1.35 \times 10^{-18} \text{ m}^2 \quad (A9)$$

is used here.

Viscosity,  $\mu$  may then be written as

$$\mu = \frac{5\pi}{32} \frac{m_A U_A}{Q_{AA}} \frac{1 + \frac{\alpha}{1-\alpha} \frac{Q_{A1}}{Q_{AA}}}{1 + \frac{\alpha}{1-\alpha} \frac{Q_{A1}}{Q_{AA}} + \frac{\alpha}{1-\alpha} \frac{Q_{11}}{Q_{AA}}} \quad (A10)$$

following Ref. A2. Any contributions made to viscosity by the electrons are neglected.

In Eq.(A10) the mean thermal atomic speed  $U_A$  is given by

$$U_A = \left[ \frac{8 kT}{\pi m_A} \right]^{1/2}$$

The total thermal conductivity  $K_{TOT}$  is given by the mixture rule

$$K_{TOT} = \frac{K_A}{1 + \frac{\alpha}{1-\alpha} \frac{Q_{A1}}{Q_{AA}}} + \frac{K_1}{1 + \frac{1-\alpha}{\alpha} \frac{Q_{A1}}{Q_{11}}} + \frac{K_e}{1 + \sqrt{2} + \sqrt{2} \frac{1-\alpha}{\alpha} \frac{Q_{eA}}{Q_{ee}}} \\ + \frac{\alpha(1-\alpha)}{2} D_A p/T \left[ \frac{5}{2} + \frac{\theta_I}{T} \right]^2 \quad (A11)$$

where  $D_A$ , the ambipolar diffusion coefficient, is

$$D_A = \frac{3}{4\pi} \frac{1}{Q_{A1}} \left( \frac{\pi kT}{m_A} \right)^{1/2}$$

and  $n$  is the total number density ( $n = n_e + n_i + n_A$ ). In Eq.(A11)  $K_A$ ,  $K_1$  and  $K_e$  are the partial coefficients for the atom, ion and electron species, respectively. In Ref. A5 their values are given as

$$K_A = 5.80 \times 10^{-7} T^{0.75} \text{ cal/cm sec}^0 \text{ K}$$

$$K_1 = 2.51 (m_e/m_A)^{1/2} K_s$$

$$K_e = 2.51 K_s$$

where  $K_s$ , the thermal conductivity of the fully ionized gas is

$$K_s = 3.55 \times 10^{-17} T n_e^{1/2} \text{ cal/cm sec}^{\circ}\text{K}$$

The electron-atom average momentum transfer cross-section,  $\sigma_{eA}$  may be obtained by curve fitting data given by Ref. A6.

#### References

- A1) Kuiper, R. A. SUDAAR No.353, Dept of Aeronautics & Astronautics, Stanford University (1968)
- A2) Knöös, S. J. Plasma Physics, 2, 207 (1968)
- A3) Amdur, I. J. Phys. Fluids, 2, 370 (1958)  
Mason, E.
- A4) Rose, D. J. "Plasmas and Controlled Fusion", M.I.T. Press and John Wiley & Sons Inc, pp.162 (1961)  
Clark, M.
- A5) Yanow, G. Ph.D. Thesis, Australian National University
- A6) Devoto, R. S. J. Phys. Fluids, 10, 354,(1967).

## APPENDIX B: ALIGNMENT OF INTERFEROMETER AND LIGHT SOURCE

With the use of interferometry for the study of boundary layers, the importance of precise alignment of the instrument and its light source, with respect to the surface of interest, is critical. Any misalignment of the light beam with respect to the surface results in the formation of spurious fringe shifts at the wall, which interferes with accurate evaluation of the interferogram in the boundary-layer region.

The Mach-Zehnder interferometer used in this experimental study is well described in Ref. B1. It is a relatively large piece of equipment (as can be seen from Fig. 3), having a 9-inch diameter field of view. Consequently some care is required in obtaining correct adjustment of it with respect to the shock tube test section.

The procedure adopted is described here step by step (with reference to Figs. 5 & 9). A gas laser is used to provide a low intensity monochromatic light source. Input to the interferometer is via a plane mirror  $M_1$ .

i) Both the laser and interferometer are crudely adjusted so that the laser beam passes approximately through the centre of the elements of the interferometer and through the centre of the area of interest in the test section, i.e., just above the shock tube floor and midway along the visible portion of it.

ii) Cross-hairs are fixed on the first parabolic mirror  $P_1$ , so that the laser beam is centered on them. A set of cross-hairs is then positioned on the second parabolic mirror  $P_2$ , centered at the corresponding point on the mirror as the first set.

iii) The focal point of  $P_1$  is located using a portable white light source clipped to the front of the iris,  $I_1^1$  (which is attached to the interferometer), the reflections of the point source from the test section and compensating chamber windows being brought to a focus on the iris. The positions of the reflections with respect to the centre of the iris are noted and the following steps are taken:

iv) The gas laser is now adjusted so that the beam passes through the centre of the iris onto the cross-hairs of  $P_1$ .

v)  $P_1$  is adjusted to direct the beam onto the cross-hairs of  $P_2$  (which results in the changing of position of the focal point of  $P_1$  since the incident beam to  $P_1$  is off-axis).

Steps (iii) to (v) are repeated until the reflections on  $I_1^1$  are centered as closely as possible.

At this point one should ensure that the beam is still centered through the required part of the test section. It may be necessary to move the interferometer and light source laterally and vertically to re-centre the beam through the test section.

Assuming that the interferometer is in adjustment for producing white light fringes (the procedure for which is described in Ref. B1), a strong white light point source is placed at the position of  $I_1^1$  and the fringes focussed on a screen placed at the image focus plane of  $P_2$ , as described in Sec. 3.3.4.

The white light source is then replaced by the gas laser and a lens  $L_1$  positioned to focus the beam to a point at  $I_1$ .

Spurious fringes at the wall indicate that the interferometer is mis-aligned in pitch. This may be corrected by adjustment of the jacks or the tire pressures of the pneumatic tires on which the interferometer stands. Any adjustment of the interferometer in this manner requires that the light source be re-adjusted so that the laser beam passes through the iris centre onto the first set of cross-hairs.

The camera is now positioned so that the beam, which exits the interferometer via the plane mirror  $M_4$ , passes through the centre of its shutter and the components of the camera are positioned accordingly, so that the beam is directed to the centre of the film plate holders. Using a white light source the camera is focussed in the desired plane (see Sec. 3.3.4) and the fringes focussed in that plane by remote control of the motor driver splitters ( $S_1$  and  $S_2$ ) and the plane mirror  $M_3$ .

The pulsed laser is aligned by means of cross-hairs attached to both ends of it, they being centered on the optical axis of the ruby lasing element.

Polaroid snapshots are taken (Fig. B1) to ensure that a satisfactory alignment has been achieved. The 3471.5A component fringes are focussed in the camera by a trial and error method of moving the film holder and taking several polaroid snapshots until the sharpest focus of the 'invisible' fringes is obtained.

#### References

- B1) Hall, J. G. University of Toronto, Institute for Aerospace Studies, Report No.27 (1954).

## APPENDIX C: ANALYSIS OF INTERFEROGRAMS

The task of reducing an interferogram, which basically consists of lines of constant order of interference, to useful information about particle density (atom, ion or electron), is a somewhat tedious one, but accuracy at this stage is essential to the overall success of an experiment.

The degree of difficulty and the amount of error which is acceptable, varies with the particular region of flow being explored and the amount of time available for the data reduction process. In this experimental program two basic regions were investigated, i) the shock wave structure, both in the free-stream and in the neighbourhood of the wall and ii) the equilibrium boundary layer region behind the shock wave. For the former case, which is essentially a 2-dimensional problem, when wall effects are considered, density gradients are experienced both parallel to the flow direction and perpendicular to it. Whereas in the equilibrium boundary layer region where one assumes constant free-stream flow conditions, we have at any given station,  $x$ , a one-dimensional problem with density changes perpendicular to the wall along  $y$ . Consequently, it was found to be convenient to employ two methods for analyzing the interferograms, which will be described here.

For parallel fringe interferometry, the equation relating refractive index  $n$  at a point  $(x,y)$  to fringe order  $N$  is (Ref. C1)

$$n(x,y) \frac{L}{\lambda} + \frac{1}{\lambda} \left[ \left( \frac{x}{d} + \text{const.} \right) - n_0 L \right] = N(x,y) \quad (\text{C1})$$

where  $L$  is the test section width,  $\lambda$  is wavelength of light,  $d$  is fringe spacing (taken from the no-flow interferogram) and the suffix '0' denotes reference region values.

Equation (C1) is valid for any general point  $(x,y)$  in the flow field. Considering now a reference point  $(x_0, y_0)$  then we may write

$$n(x_0, y_0) \frac{L}{\lambda} + \left[ \left( \frac{x_0}{d} + \text{const.} \right) - n_0 L \right] = N(x_0, y_0) \lambda \quad (\text{C2})$$

Subtracting (C2) from (C1) gives

$$\left[ n(x,y) - n(x_0, y_0) \right] \frac{L}{\lambda} = N(x,y) - N(x_0, y_0) - \frac{(x-x_0)}{d} \quad (\text{C3})$$

At this point it is pertinent to discuss the initial orientation with which the fringes are pre-set. The two basic choices are to have the fringes set parallel to the direction of the density change or perpendicular to it. The former gives the most information since one has a continuous trace of refractive index in the direction of the changes while the latter gives only discrete points but is much simpler to evaluate. In the shock wave region there is no well defined point or region at which the flow conditions are known, as required by Eq.(C3). One could assume the frozen flow values predicted by theory for the region immediately behind the shock front. However the pre-shock gas state is well known from laboratory measurements, so this may be used as a good reference region. In order to

use the undisturbed gas as a reference, the fringes should be orientated so as to pass through the shock front, making horizontal fringes most appropriate. However, in the boundary layer region at the wall it is desirable to have the fringe orientated vertically. Consequently a compromise between these two requirements is best obtained by using diagonally orientated fringes.

Looking now at Eq.(C3) in context with Fig. C1 we see that the refractive index  $n$  at point  $(x,y)$  in the flow field may be obtained by the following procedure:

i) Select a fringe in the no-flow field to use as a reference. Arbitrarily set the fringe order (e.g.,  $N = 1$ ) since it is  $\Delta N$  that we are interested in.

ii) For  $y = y_0$ , measure  $x - x_0$  and calculate  $\Delta N$  (in this case, 1), being careful with the sign of  $\Delta N$ .

iii) Measure  $d$ , the no-flow fringe spacing (in  $x$  co-ord. direction).

iv) Substitute the above values in Eq. C3 to obtain  $n(x,y) = n(x_0, y_0)$ , ( $y = y_0$ ).

The relationship between refractive index and density is (Ref. C2)

$$n - 1 = \sum_s K_s \rho_s \quad (C4)$$

where  $K_s$  is the Gladstone-Dale constant for species 's' and  $\rho_s$  is the density of species 's'. When expanded for the case of a singly ionized plasma, neglecting contributions to refractive index from excited states, Eq. C4 becomes (in c.g.s. units)

$$(n_j - 1) - (n_{j_1} - 1) = K_A (\rho_j - \rho_{j_1}) - (\rho_j \alpha_j - \rho_{j_1} \alpha_{j_1}) (K_A - K_I + 0.67 \cdot 10^9 \lambda^2) \quad (C5)$$

where '1' denotes reference value, 'j' the unknown value and  $K_A$  and  $K_I$  are the Gladstone-Dale constants for atoms and ions respectively.

From Eq.C5 we see the requirement for two similar equations (one each for  $\lambda_1$  and  $\lambda_2$ ) to be solved simultaneously for  $\rho_j$  and  $\alpha_j$ .

If we let

$$N_1 = [(n_{j_1} - 1) - (n_{j_1} - 1)]$$

and

$$N_2 = [(n_{j_2} - 1) - (n_{j_2} - 1)]$$

then algebraic manipulation of the two equations (C5) yields

$$\rho_j = \rho_1 + \frac{N_2 c_1}{K} - \frac{N_1 c_2}{K} \quad (C6)$$

and

$$\alpha_j = \left[ \rho_1 \alpha_1 - \frac{K_{A_2} N_1}{K} + \frac{K_{A_1} N_2}{K} \right] / \rho_j \quad (C7)$$

where

$$c_1 = 0.33 K_{A_1} + 0.67 \times 10^9 \lambda_1^2$$

$$c_2 = 0.33 K_{A_2} + 0.67 \times 10^9 \lambda_2^2$$

$$K = c_1 K_{A_2} - c_2 K_{A_1}$$

and  $K_1 = 0.67 K_A$  (Refs. C2 and C3).

For the light-source wavelengths used in these experiments ( $\lambda_1 = 6943 \text{ \AA}$ ,  $\lambda_2 = 3471.5 \text{ \AA}$ ) the constants take the following values

$$\begin{aligned} K_{A_1} &= 0.15726 \text{ cm}^3/\text{gm} & K_{A_2} &= 0.16273 \text{ cm}^3/\text{gm} \\ c_1 &= 3.2816 \text{ cm}^3/\text{gm} & c_2 &= 0.8611 \text{ cm}^3/\text{gm} \\ K &= 0.3986 \text{ cm}^6/\text{gm}^2 \end{aligned}$$

Hence with the values of  $N_1$  and  $N_2$  taken from the two interferograms using Eq.C3 one can obtain  $\rho$  and  $\alpha$  from Eqs. C6 and C7.

For the equilibrium flow boundary layer region the following procedure was adopted.

Using fringes orientated perpendicular to the wall, the change in density through the boundary layer is characterized by a shifting or bending of the fringes to the left or right (depending on how the interferometer is adjusted). Taking the free stream flow as our reference, the equilibrium conditions being predicted by strong-shock real gas theory, a no-flow interferogram is used to obtain the undisturbed gas fringe path to the wall and then using this in conjunction with the flow interferogram, the fringe shift may be determined at any point on a fringe.

The relationship between the non-dimensional fringe shift  $S_{1j}$  (non-dimensionalized by the no-flow fringe spacing) and change in refractive index is (Ref. C1)

$$S_{1j} = \frac{L}{\lambda} [(n_j - 1) - (n_1 - 1)] \quad (C8)$$

Referring to Fig. C2, the nondimensional shift  $S_{1j}$  is determined in the following manner:

i) For the point of interest ( $x, y$ ) the average  $x$  co-ordinate difference in the uniform flow region between the flow fringe on which the point lies and the nearest no-flow fringe, is determined ( $\Delta x$ ).

ii) At the same  $y$  co-ordinate ( $y = y_0$ ) the  $x$  co-ordinate difference between the flow and no-flow fringes in the boundary layer is measured ( $x - x_0$ ).

iii) The non-dimensional shift  $S_{ij}$  is then calculated as

$$S_{ij} = \frac{x - x_0 + \Delta x}{d}$$

for the point ( $x, y$ ), where  $d$  is the average no-flow fringe spacing.

An equation similar in form to Eq. C5 may be obtained as

$$S_{ij} = \frac{L}{\lambda} [K_A(\rho_j - \rho_i) - (\rho_j \alpha_j - \rho_i \alpha_i) (K_A - K_I + 0.67 \times 10^9 \lambda^2)] \quad (C9)$$

(in c.g.s. units)

with corresponding equations for  $\rho$  and  $\alpha$  being

$$\rho_j = \rho_i - \frac{\lambda_1 c_2 S_1}{KL} + \frac{\lambda_2 c_1 S_2}{KL} \quad (C10)$$

$$\alpha_j = \left[ \alpha_i \alpha_i - \frac{\lambda_1 K_A S_1}{KL} + \frac{\lambda_2 K_A S_2}{KL} \right] / \rho_j \quad (C11)$$

where  $L$  is the test section width taken as  $L = 10.16$  cm, the other constants taking on the same values as for Eqs. C6 and C7.

Thus having obtained values of  $S_1$  and  $S_2$  at a point ( $x, y$ ), the densities ( $\rho$  and  $\alpha$ ) at that point may be calculated from Eqs. C10 and C11.

Some points should now be made concerning the practical application of the described methods of analysis.

The most important is that the values of  $N_1$  and  $N_2$  or  $S_1$  and  $S_2$  may only be determined from the interferograms at points ( $x, y$ ) which actually lie on a flow fringe since it is convenient to use fringe centres as references of constant intensity. The fringe pattern for each wavelength is of course different and the probability of a point ( $x, y$ ) chosen for a fringe at one wavelength, lying on a fringe in the other wavelength, is very small. Consequently an interpolation routine is required to determine the values of  $N_1$  and  $N_2$  or  $S_1$  and  $S_2$  at points between fringes.

A Ruscom digitizer (Model 21), measuring in hundredths of an inch, was used to obtain ( $x, y$ ) co-ordinate data for each fringe of an interferogram. This data (punched onto computer cards) was then used with a computer program written (for the UTIAS IBM 1130 computer) to (see Fig. C3),

i) Linearly interpolate the digitized x,y co-ordinates in steps of y ( $\Delta y = 0.05$  mm in lab. co-ord).

ii) Compute  $N_1$  and  $N_2$  or  $S_1$  and  $S_2$  at interpolated x,y co-ordinates.

iii) Linearly interpolate between two nearest data points lying either side of required x station, at each step value of y for each wavelength.

iv) Calculate  $\rho$  and  $\alpha$  from interpolated values of  $N_1$  and  $N_2$  or  $S_1$  and  $S_2$  at each point (x,y).

The importance of correctly determining the true wall position (as mentioned in Sec. 3.3.4) to the accuracy of  $\rho$  and  $\alpha$ , may be appreciated here. Any error in the wall location for one wavelength interferogram results in the values of N or S being assigned the wrong (x,y) values for that interferogram. Estimates of the errors involved in calculated values of  $\rho$  and  $\alpha$  due to wall location errors are given in Sec. 4.3.

One basic difference between the methods employed is the use of the no-flow interferograms, taken for each experiment prior to the run. The purpose of these interferograms is to eliminate any fringe distortions due to optical imperfections of the interferometric system. For the method used to evaluate the equilibrium boundary layer region, the no-flow interferogram was employed as previously described. However, for the shock-wave region it was found impractical to use the no-flow interferograms owing to the gross changes of the fringes in the field of view. But since the reference region taken in this method was a no-flow region, account was taken of any aberration (lens) effects but not of any local fringe distortions due to burns on the optical elements or diffraction caused by foreign particles. This is felt to be a minor source of error and not significant to the experimental results in a region where relatively large changes in flow properties take place.

#### References

- C1) Glass, I. I. University of Toronto, Institute for Aerospace Studies,  
Kawada, H. Report No.85 (1962).
- C2) Alpher, R. A. J. Phys. Fluids 2, 153 (1959).  
White, D. R.
- C3) Bristow, M.P.F. University of Toronto, Institute for Aerospace Studies,  
Report No. 158 (1971)

Table I. Experimental Data

$M_s$	$P_1$ (mmHg)	$S_{\lambda 1}$	$S_{\lambda 2}$	$\rho$ (Kg/m <sup>3</sup> )	$\alpha$ (%)	$\rho_{th}$ (Kg/m <sup>3</sup> )	$\alpha_{th}$ (%)
16.53	5.12	0.724	1.520	$4.314 \cdot 10^{-2}$	-6.74.10 <sup>-2</sup>	$4.380 \cdot 10^{-2}$	0.0
16.68	5.17	0.715	1.599	$4.558 \cdot 10^{-2}$	$3.52 \cdot 10^{-1}$	$4.412 \cdot 10^{-2}$	0.0
13.59	5.09	0.744	1.608	$4.525 \cdot 10^{-2}$	$2.03 \cdot 10^{-1}$	$4.328 \cdot 10^{-2}$	0.0

Table II. Shock Wave Flow Properties

$M_s = 16.53$							
	$P$ (torr)	$\rho$ (Kg/m <sup>3</sup> )	$T$ (°K)	$U$ (M/s)	$\alpha$ (%)	$n_e$ ( $/m^3$ )	
Initial (1)	5.12	0.0111	297	0	0	0	
Frozen (2)	1749	0.0438	25,588	3962	0	0	
Equilibrium (3)	2058	0.0857	13,158	4618	15.78	$2.039 \cdot 10^{23}$	

$M_s = 13.59$							
	$P$ (torr)	$\rho$ (Kg/m <sup>3</sup> )	$T$ (°K)	$U$ (M/s)	$\alpha$ (%)	$n_e$ ( $/m^3$ )	
Initial (1)	5.09	0.0110	297	0	0	0	
Frozen (2)	1175	0.0433	17,390	3253	0	0	
Equilibrium (3)	1315	0.0668	11,741	3643	7.42	$7.47 \cdot 10^{22}$	

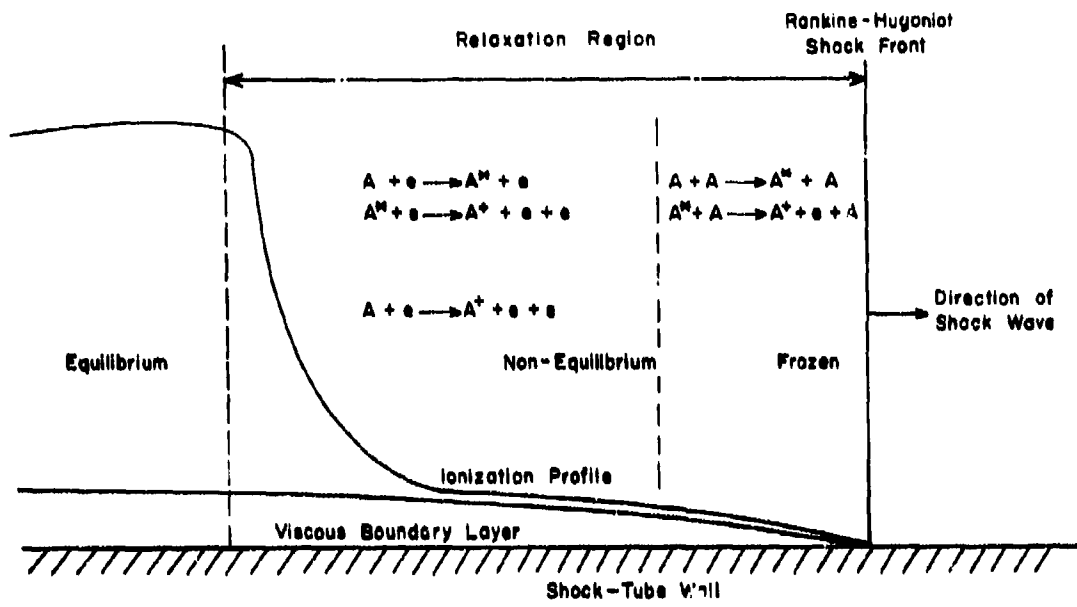
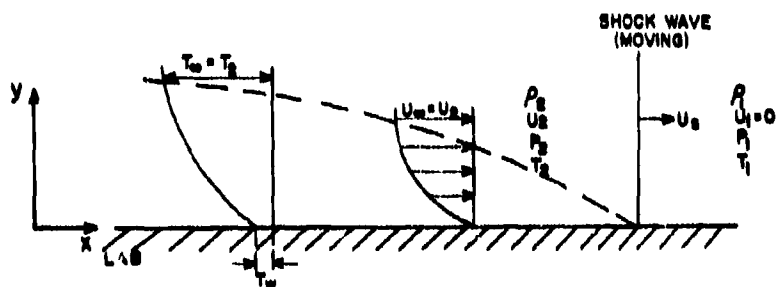
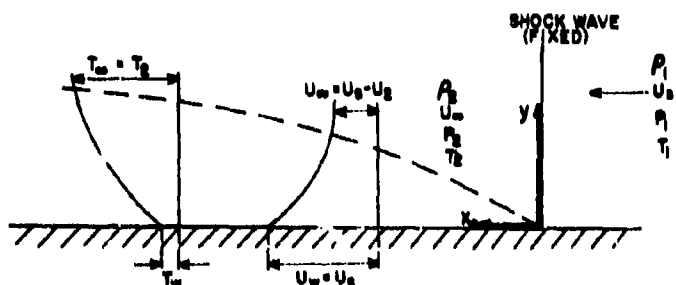


FIG. 1 DIAGRAM OF IONIZING SHOCK WAVE STRUCTURE



NONSTATIONARY CO-ORDINATE SYSTEM AT TIME  $t$



STATIONARY CO-ORDINATE SYSTEM, SHOCK WAVE FIXED IN Y-AXIS

FIG. 2 SHOCK TUBE WALL BOUNDARY LAYER CO-ORDINATE SYSTEMS

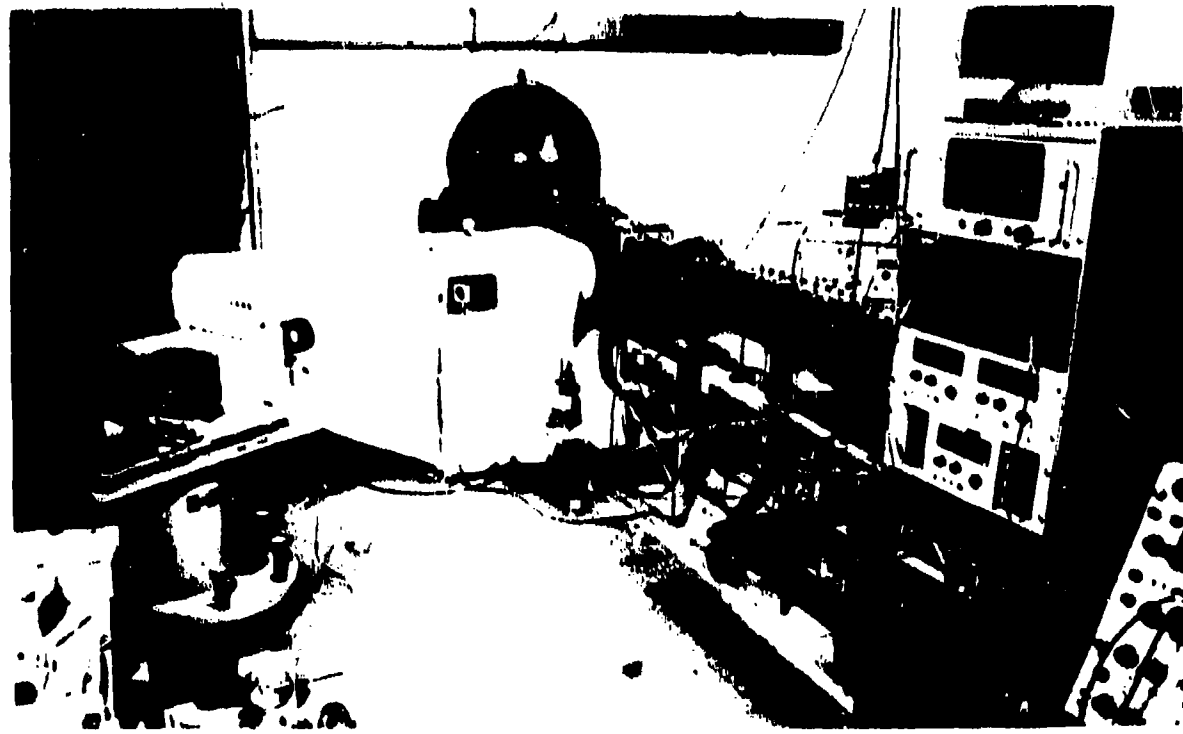
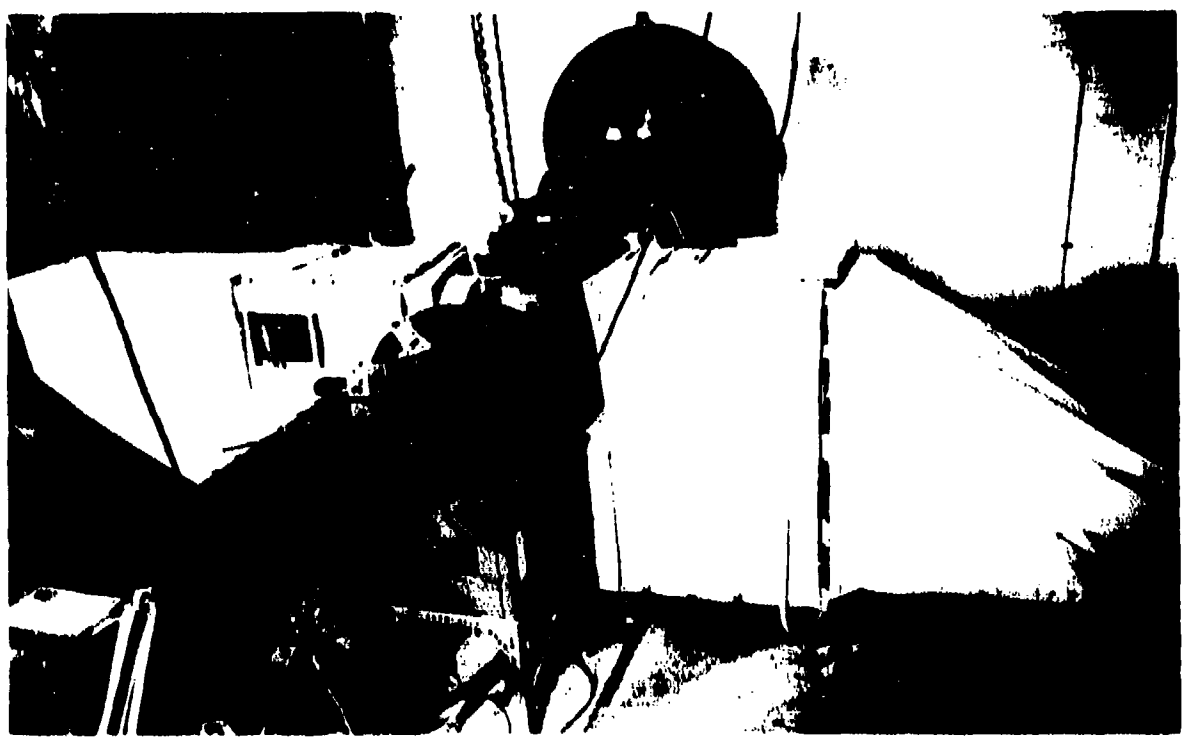
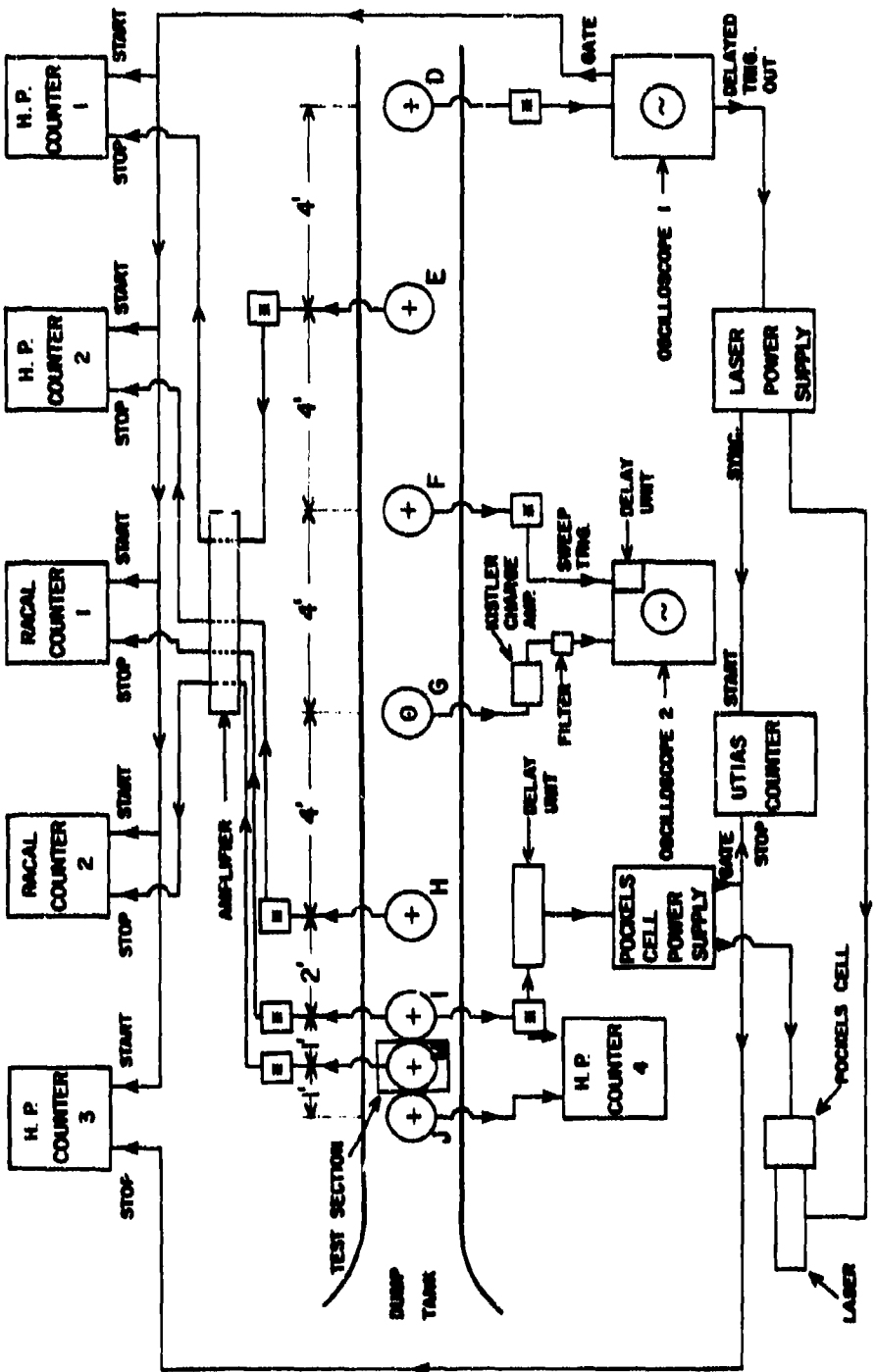


FIG. 3 TEST SECTION OF UTIAS 4" X 7" HYPERVELOCITY

SHOCK TUBE AND ASSOCIATED EQUIPMENT



## **SYMBOLS**

- ATLANTIC RESEARCH LD-25 PRESSURE TRANSDUCERS  
KESTLER TRANSDUCERS  
IMPEDANCE MATCHING UNITS

FIG. 4 SCHEMATIC CIRCUIT DIAGRAM FOR VELOCITY MEASUREMENTS & LIGHT SOURCE

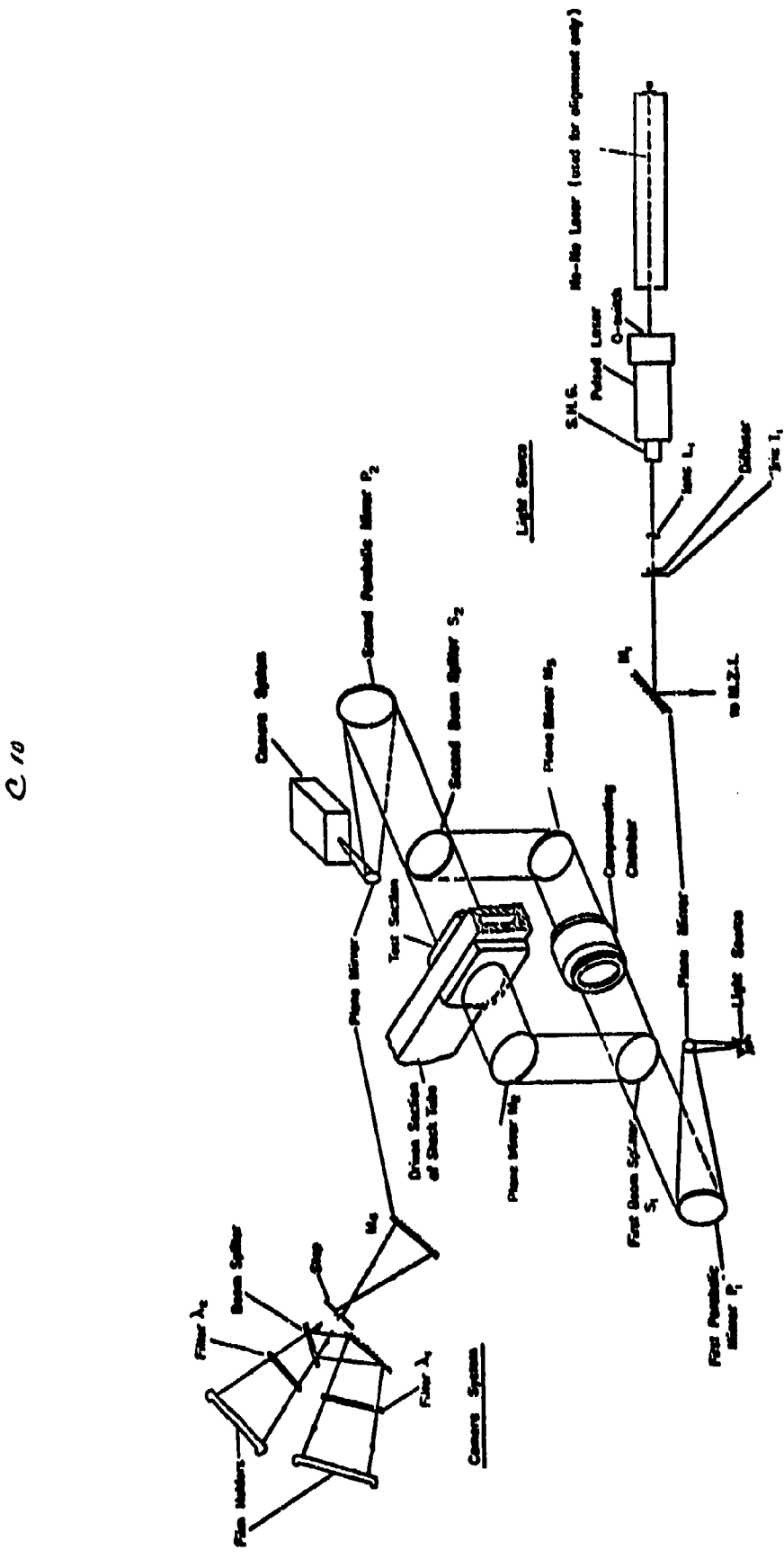


FIG. 5 DIAGRAM OF OPTICAL ARRANGEMENT

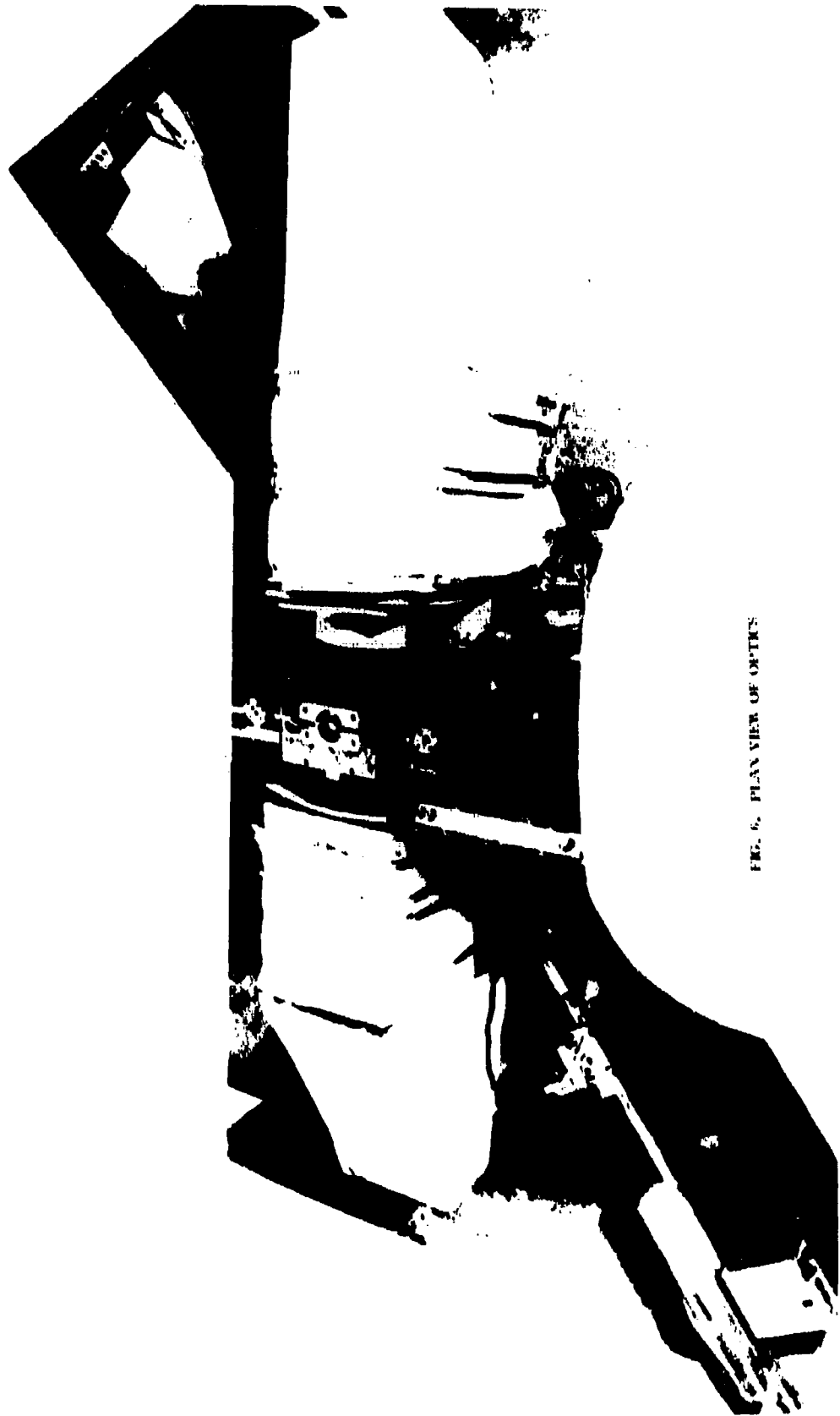
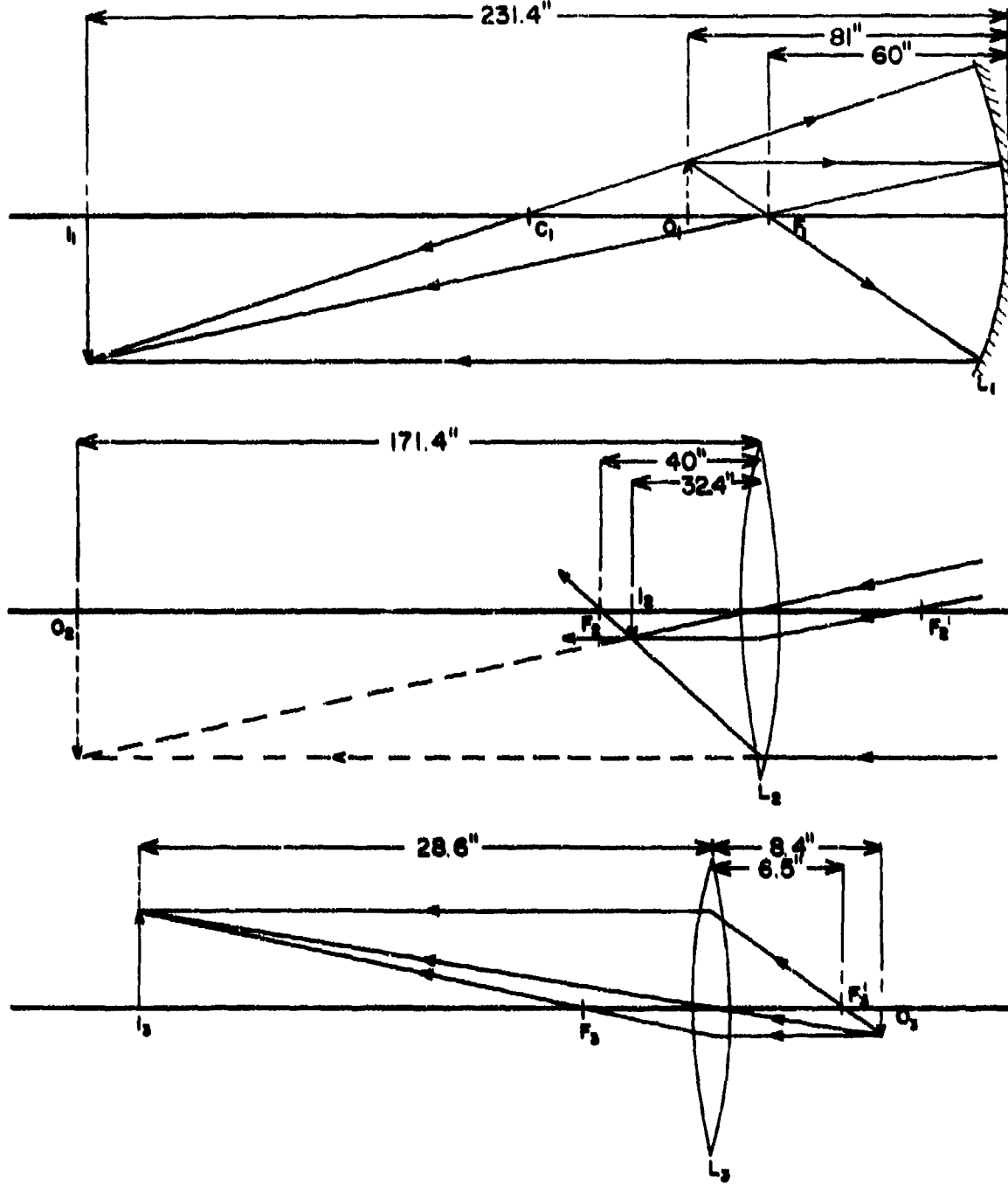


FIG. 6. PLAN VIEW OF OPTICS

CII



**O** = OBJECT POSITION  
**I** = IMAGE POSITION  
**F** = FOCUS  
**C** = CENTRE OF CURVATURE

**$L_1$**  = PARABOLIC MIRROR  
 **$L_2$**  = FIRST CONVEX LENS  
 **$L_3$**  = SECOND CONVEX LENS

FIG. 7 RAY DIAGRAM FOR INTERFEROMETER OUTPUT LENS SYSTEM



Initial Magnification = 5.0



Final Magnification = 20.0

Initial Magnification = 0.5

FIG. 8 COMPARISON BETWEEN INTERFEROGRAMS OF DIFFERENT

INITIAL MAGNIFICATION

2 / 3

C14

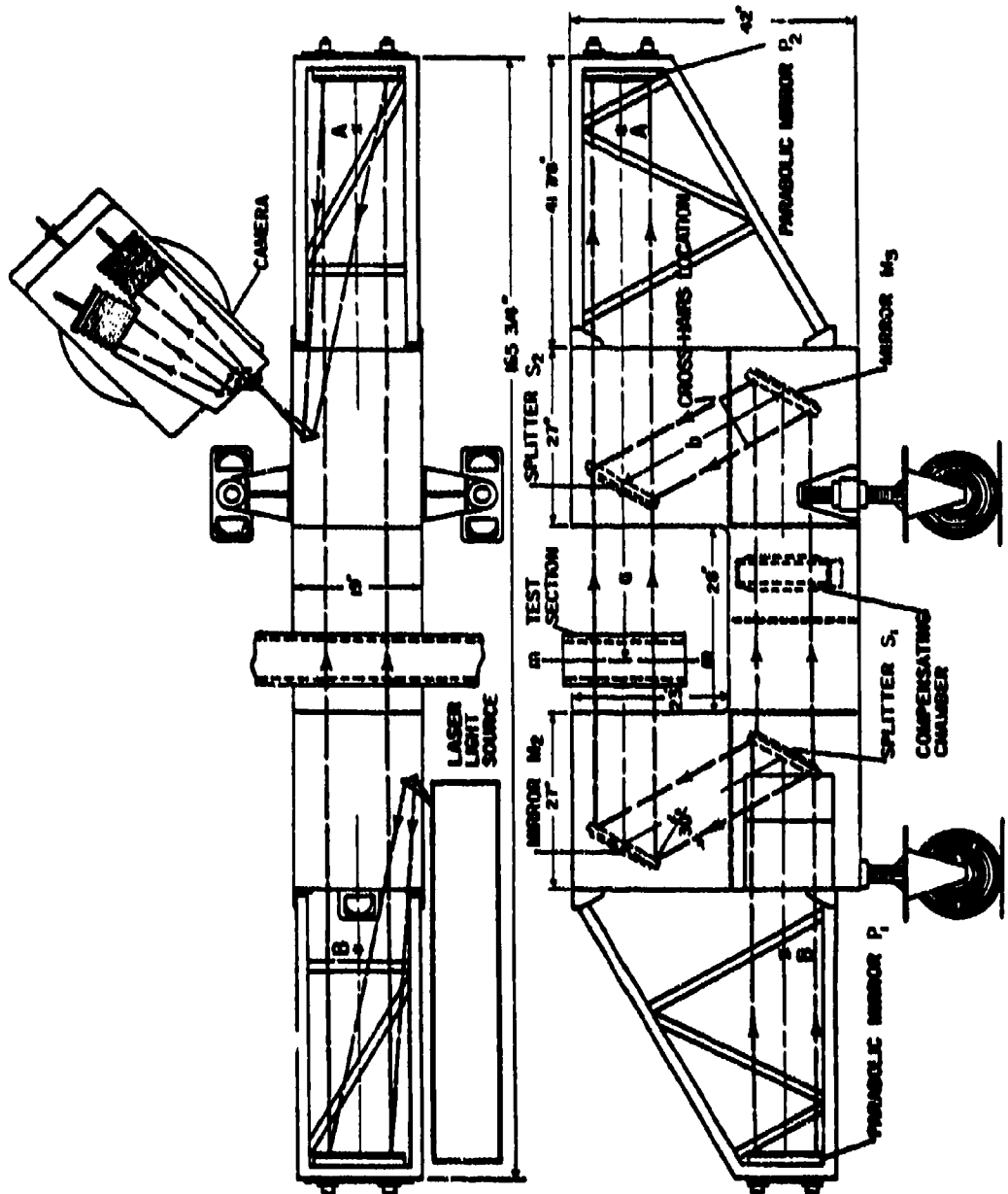


FIG. 9 SCHEMATIC OF INTERFEROMETER SHOWING  
POSITION OF CROSS-HAIRS

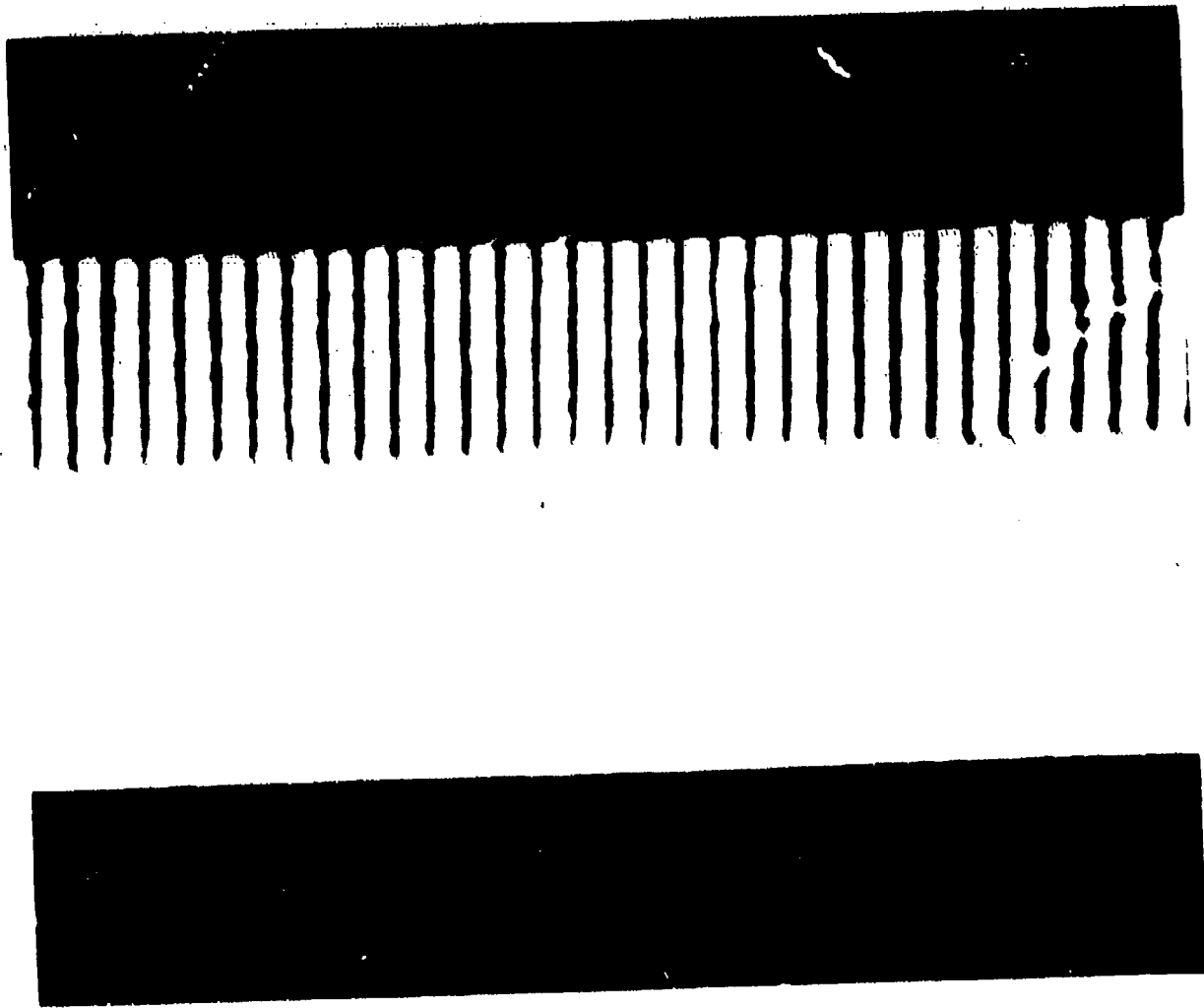


FIG. 10 TYPICAL PHOTOGRAPH FROM WHICH WALL POSITION  
MEASUREMENTS WERE TAKEN

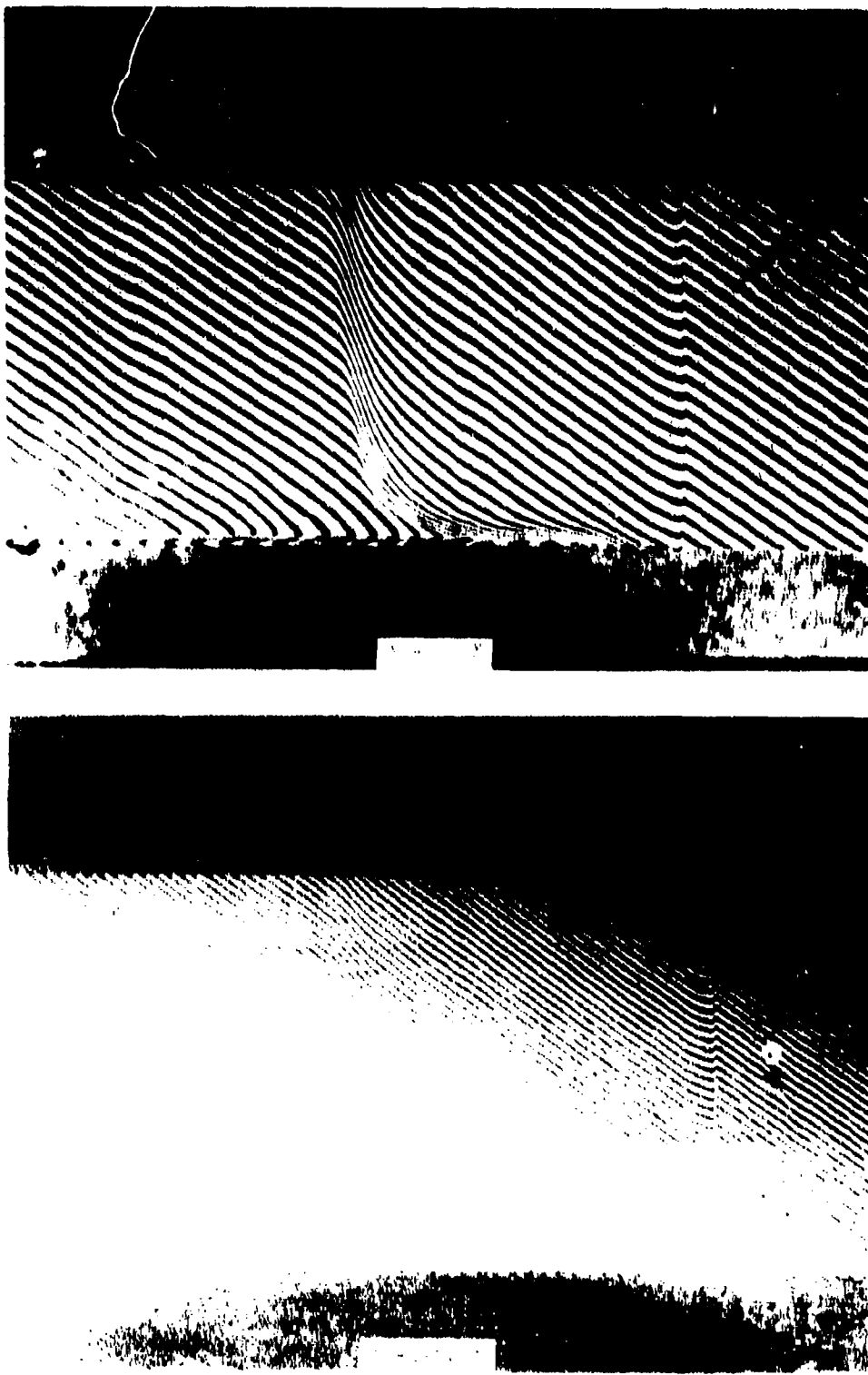


FIG. 11 INTERFEROGRAMS TAKEN SIMULTANEOUSLY OF SHOCK  $M_s = 10.53$  TRAVELLING (TO  
RIGHT) INTO PURE ARGON,  $P_1 = 5.12$  TORR., DISTANCE BETWEEN CROSS-HAIRS  
IS APPROXIMATELY 1 CM.

c. 16

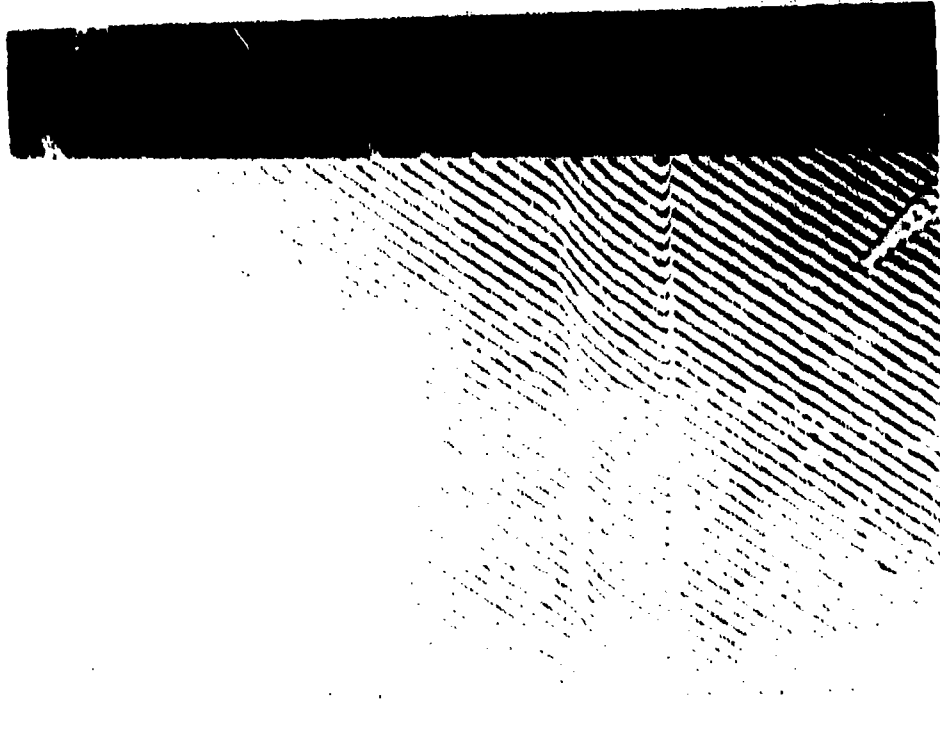
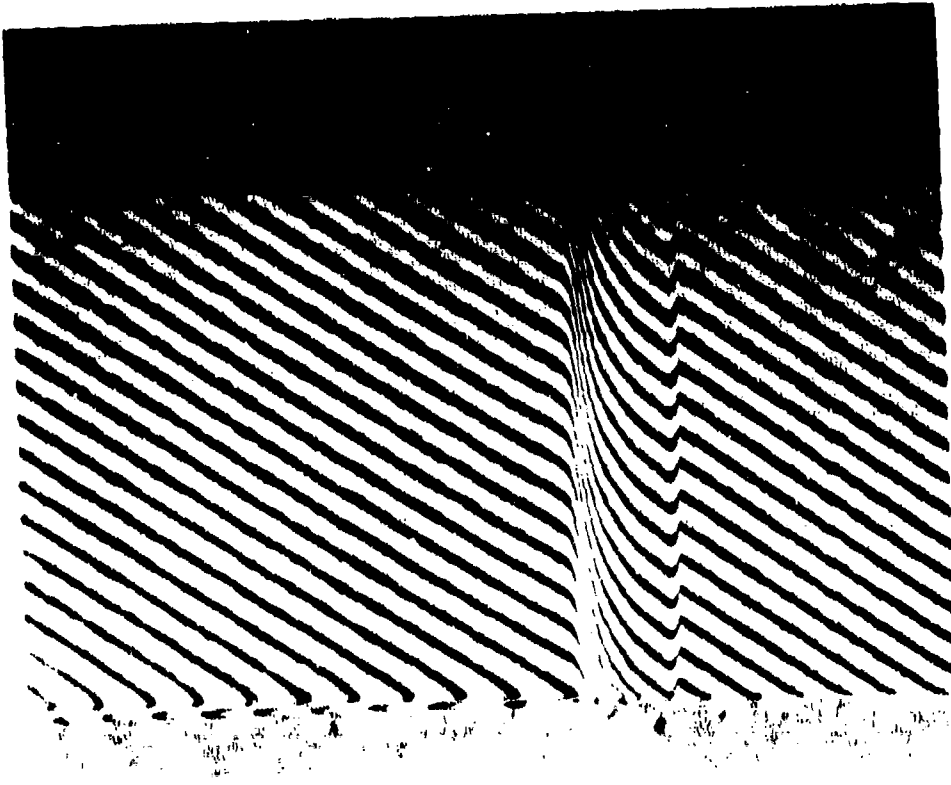


FIG. 12 INTERFEROGRAMS OF SHOCK  $M_0 = 10.63$  TRAVELLING INTO AIR WITH 0.4% HYDROGEN ADDED.  $P_1 = 5.17$  TORR.

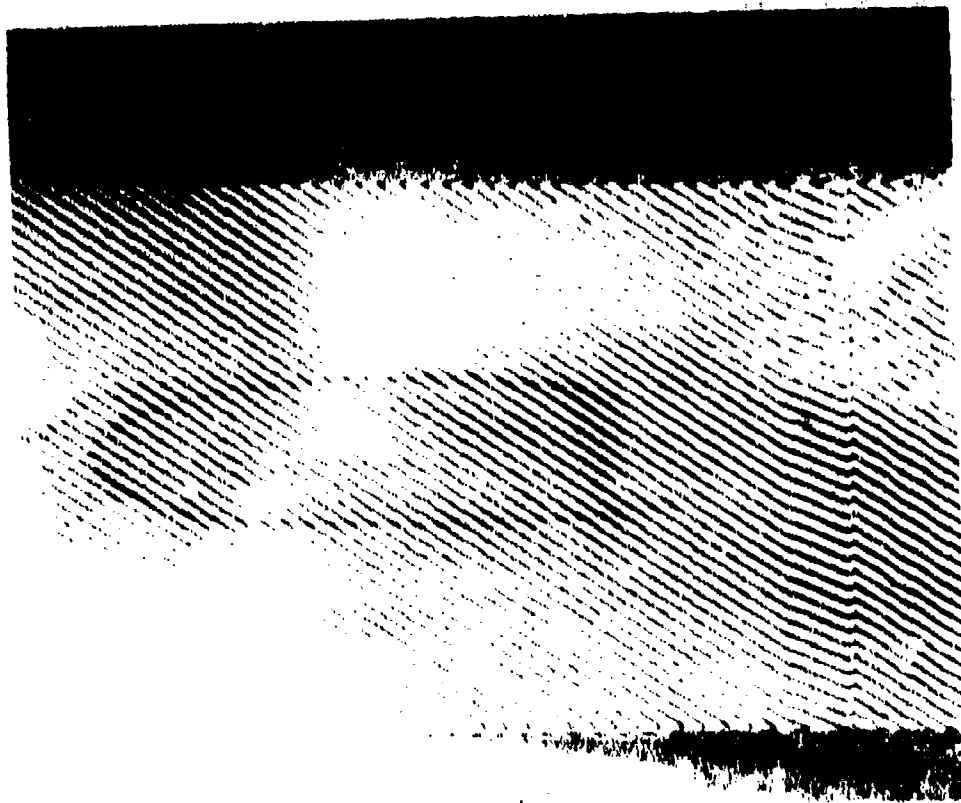
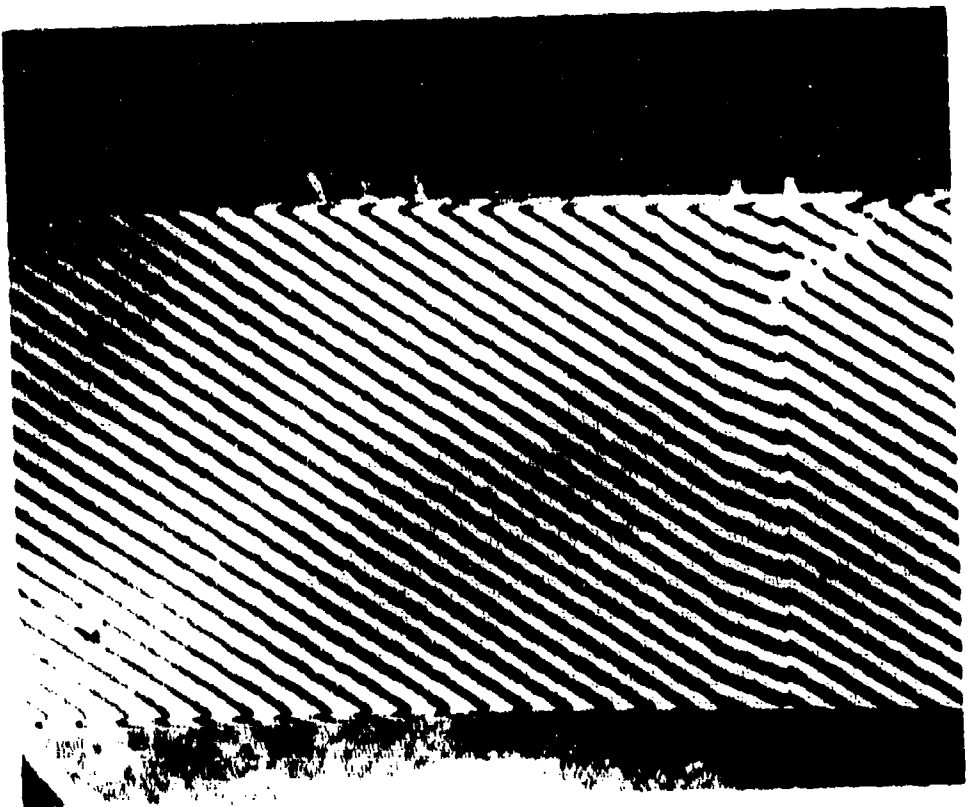
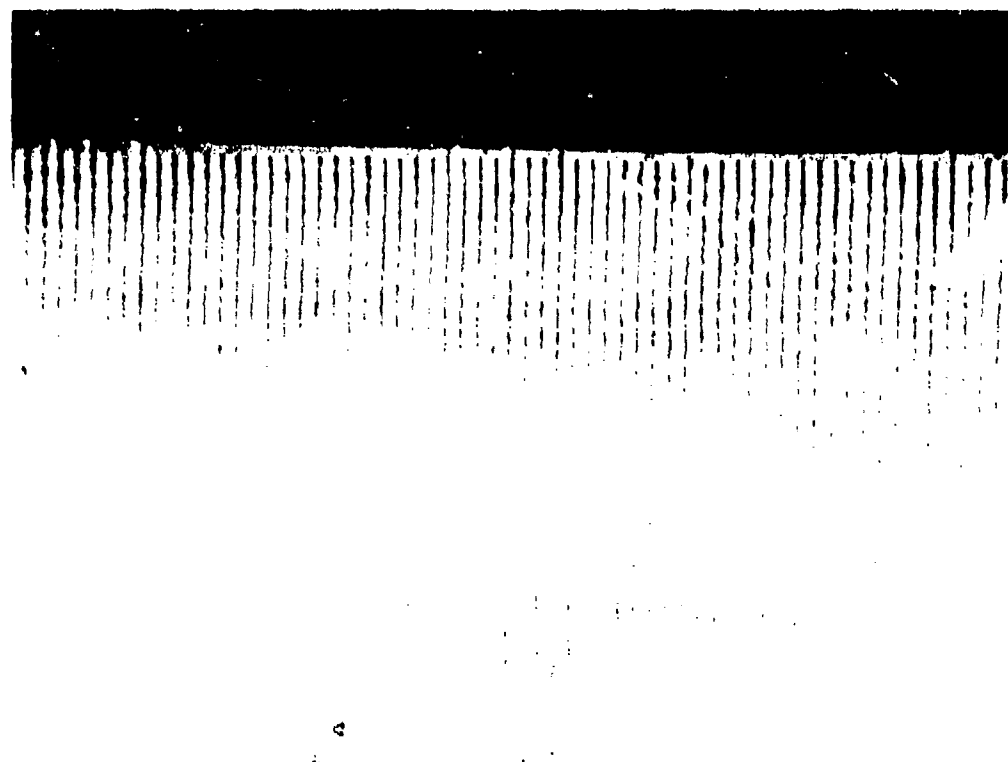
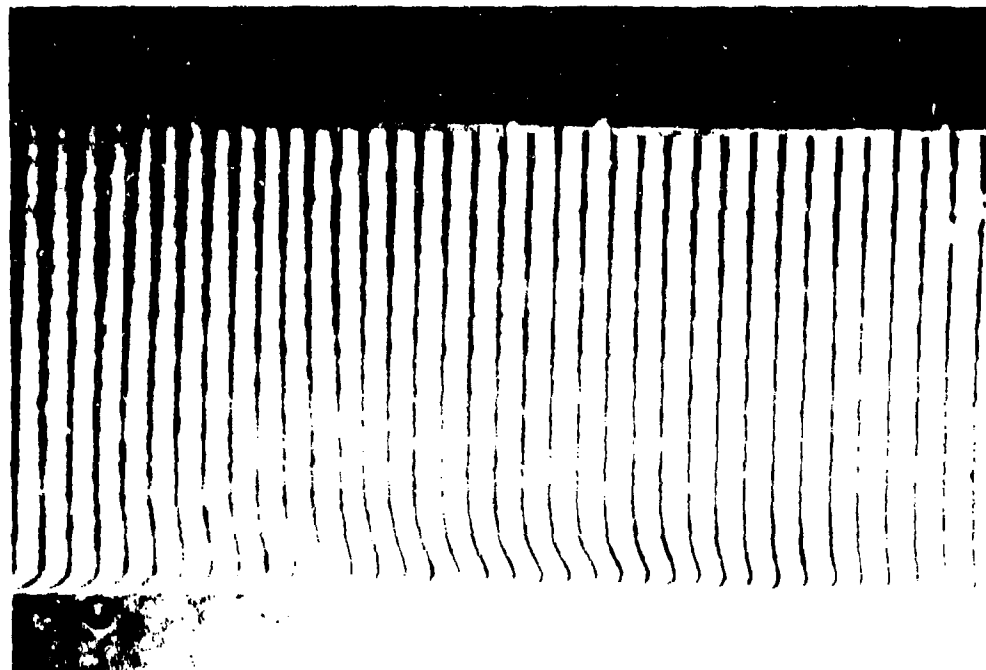


FIG. 15 INTERFEROGRAMS OF SILICONE  $A_0 = 13.50$ , TRAVELLING (TO RIGHT) INTO PURE ARGON.  $P_1 = 5.00$  TORR.

C18



Reproduced from  
best available copy.

FIG. 10. INTERFERENCE PATTERNS IN RELAXATION REGION BEHIND SHOCK.  $M_\infty = 13.59$ , TRAVELLING  
TO RIGHT INTO PURE ARGON,  $P_0 = 3.09$  TORR,  
CONTINUATION OF FIG. 13.  $\Delta X = 0.05$ .

FIG. 15 RELAXATION REGION FREESTREAM DENSITY PROFILES FOR PURE ARGON AND ARGON + 0.4% HYDROGEN

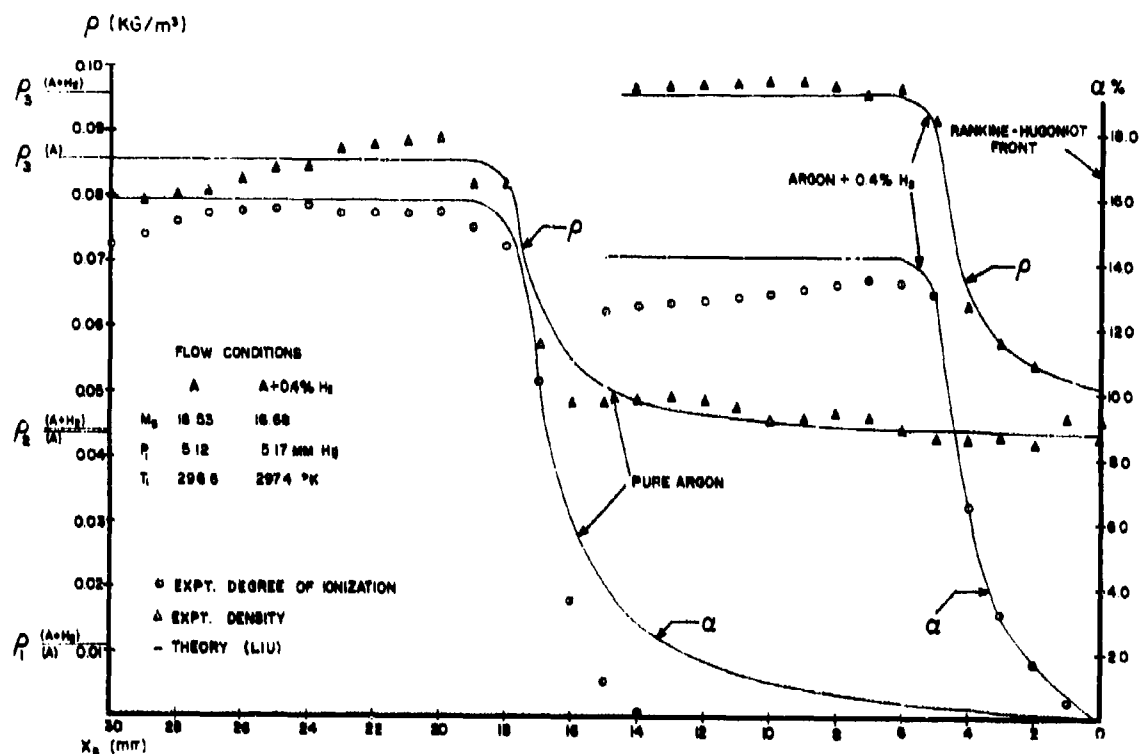
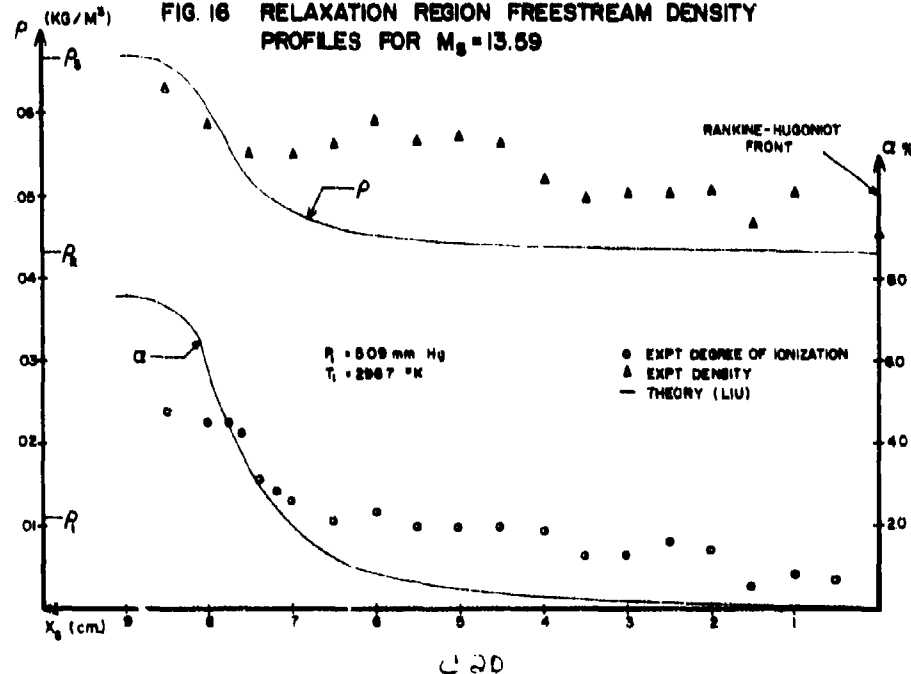


FIG. 16 RELAXATION REGION FREESTREAM DENSITY PROFILES FOR  $M_\infty = 13.59$



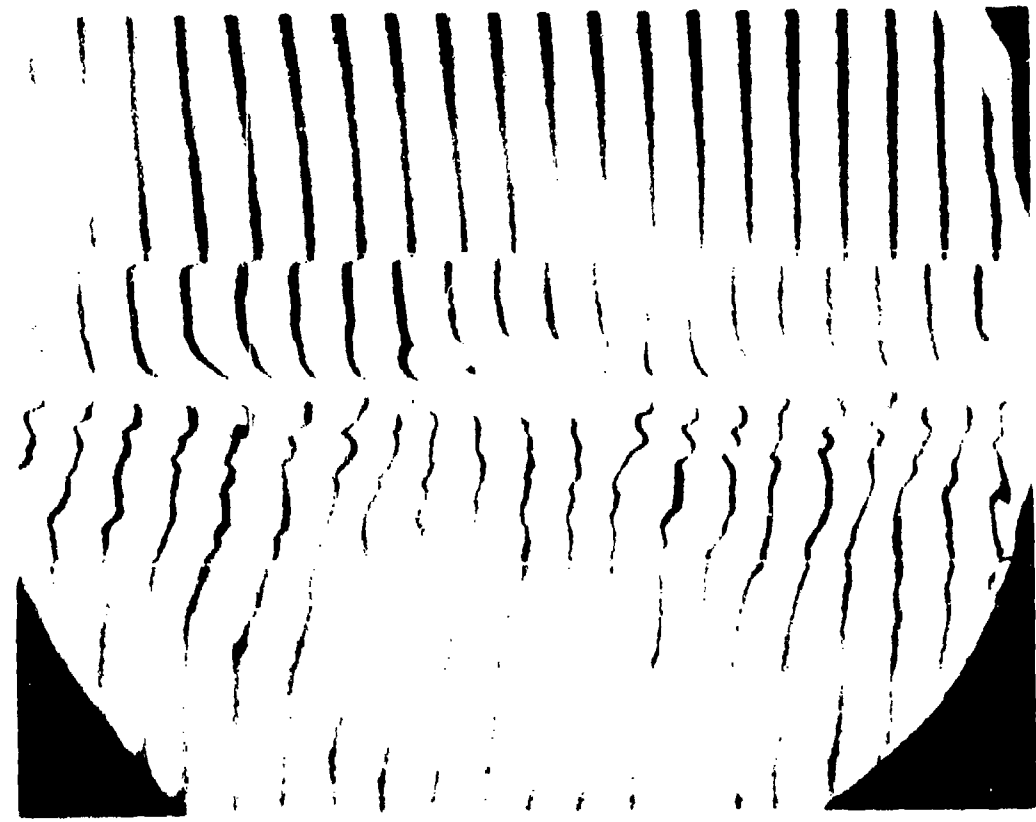
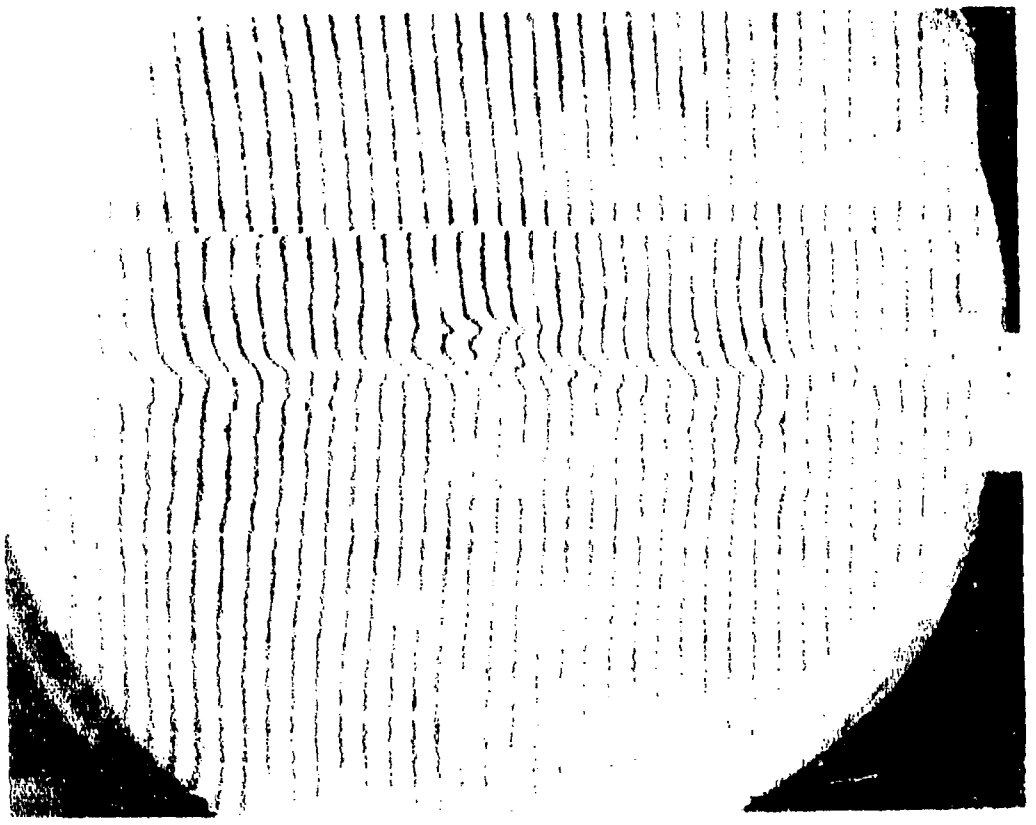


FIG. 17 HORIZONTAL FRINGE INTERFERENCES OBTAINED BY BRASTON'S SHOCK.  $\mu_s = 17.0$  TRAVELLING (TO RIGHT) INTO AIR.  $P_1 = 2.45$  MM. VERTICAL APERTURE IS 7 INCHES.

C 24

FIG. 18 CONTOURS OF CONSTANT DEGREE OF IONIZATION IN RELAXATION REGION CLOSE TO WALL FOR PURE ARGON ( $P = 5.12 \text{ mm Hg}$ ) AND  $M_\infty = 16.53$

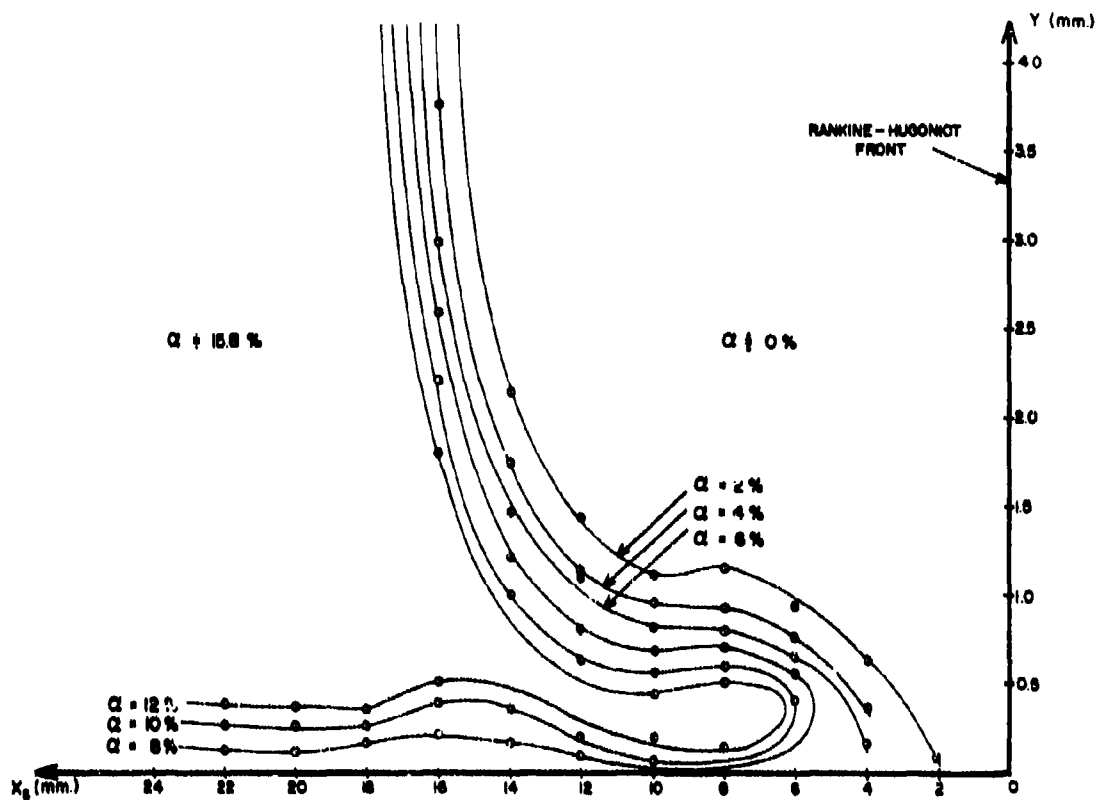


FIG. 19 CONTOURS OF CONSTANT DEGREE OF IONIZATION IN  
RELAXATION REGION CLOSE TO WALL FOR PURE  
ARGON ( $P = 509 \text{ mm. Hg}$ ) AND  $M_\infty = 13.89$

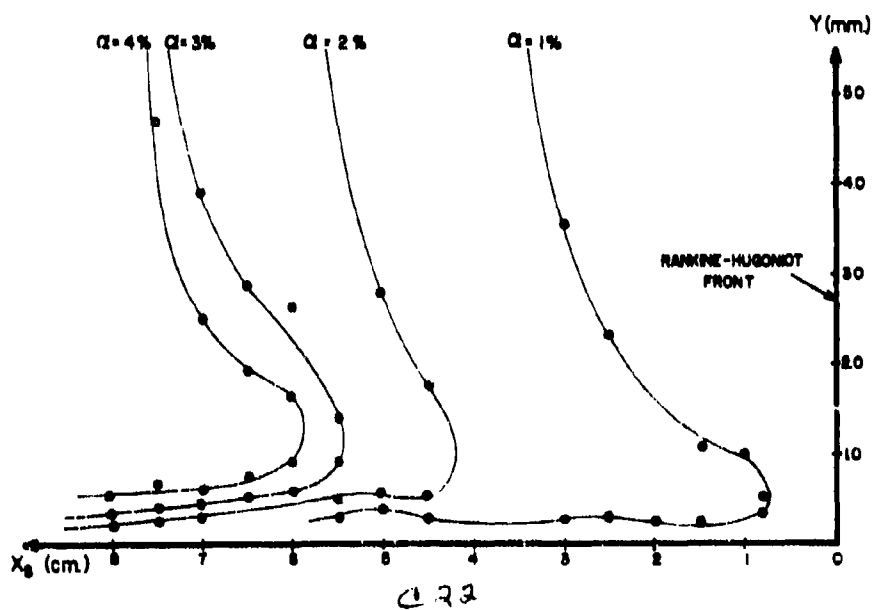
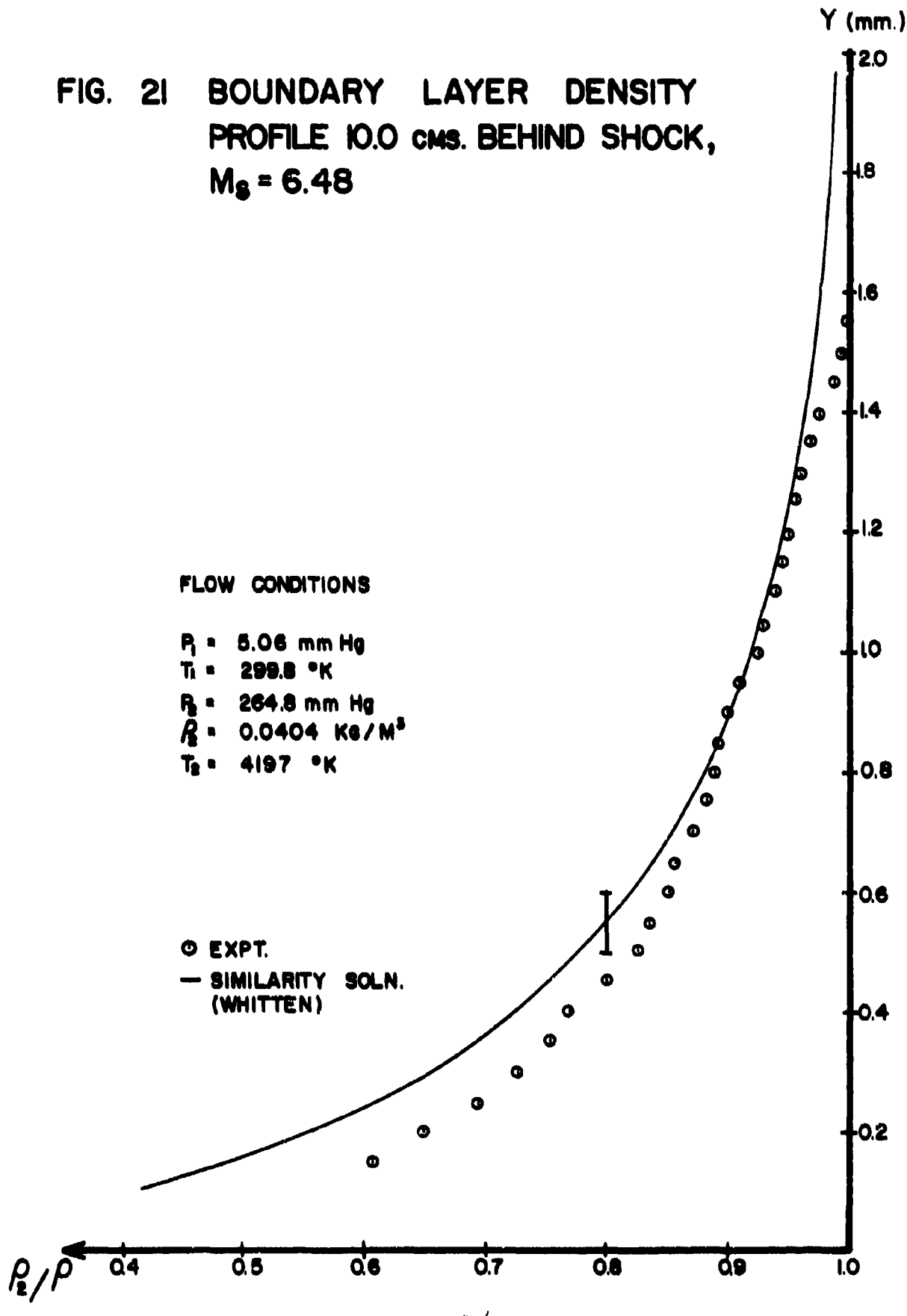




FIG. 20 INTERFEROGRAMS OF SHOCK  $U_2 = 10,41$  TRAVELLING (TO RIGHT) OVER TUNGSTEN  
FOIL INTO ARGON,  $P_1 = 5.11$  TORR.

0.23

FIG. 21 BOUNDARY LAYER DENSITY PROFILE 10.0 cms. BEHIND SHOCK,  
 $M_s = 6.48$



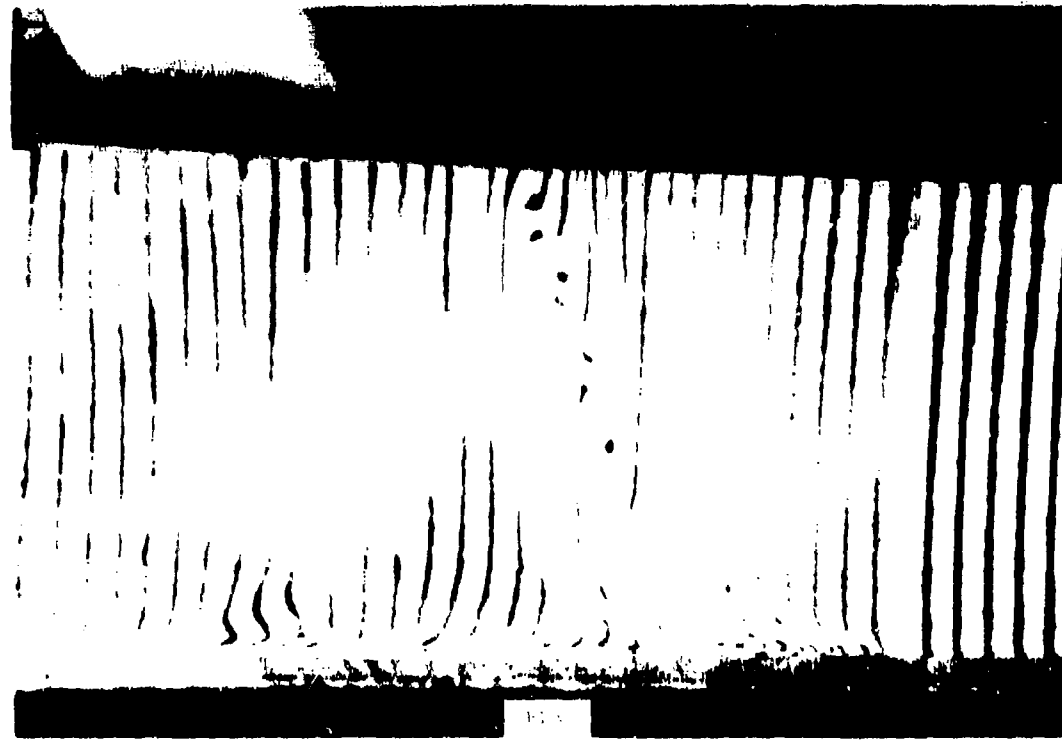
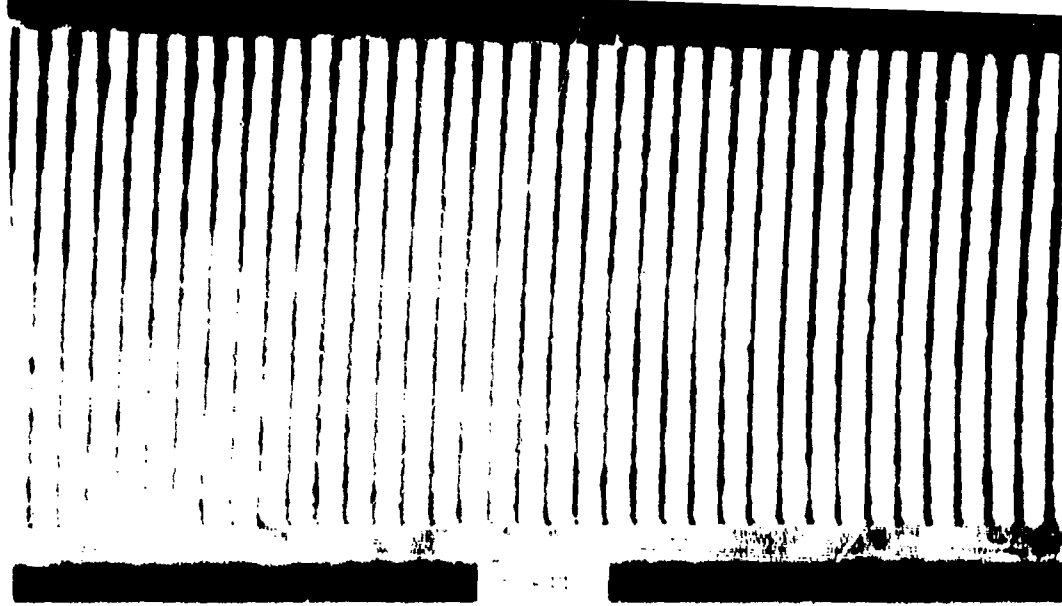


FIG. 22. PULSING 70-400 CYCLES SEC. IN 365 CM<sup>-1</sup> AND 10<sup>-3</sup> M<sup>2</sup>/S.  
TRAVELING 0.1 MM/SEC. IN 10<sup>-3</sup> M<sup>2</sup>/S.

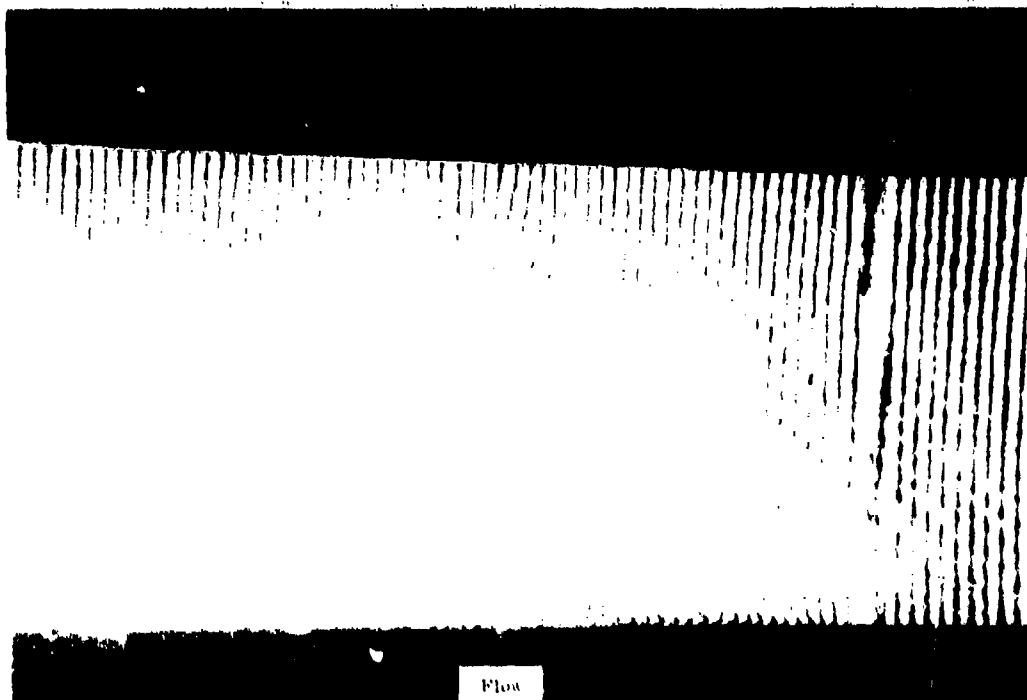
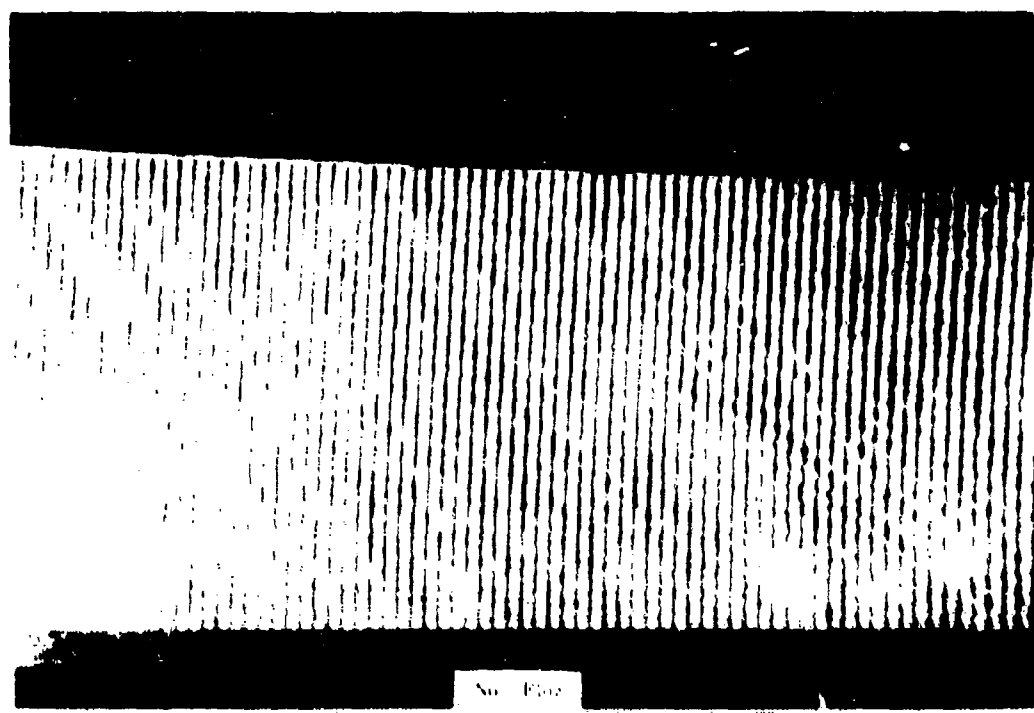


FIG. 23 FLOW AND NO-FLOW INTERFEROGRAMS ( $\lambda_2 = 3071.5$  Å) CORRESPONDING TO THOSE OF FIG. 22.

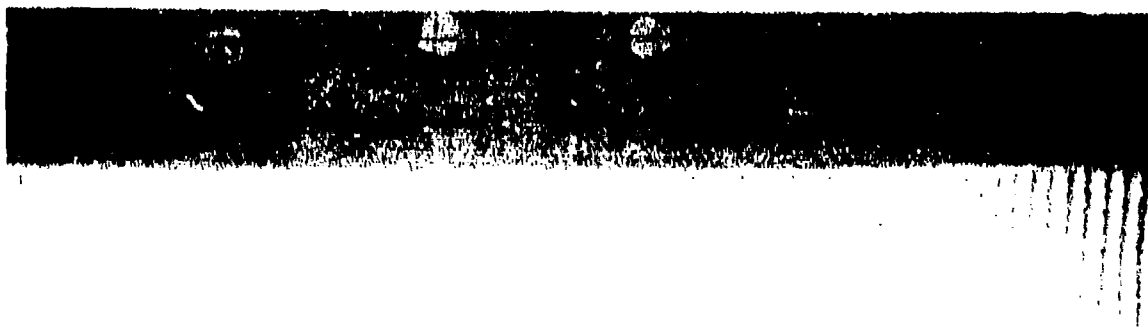
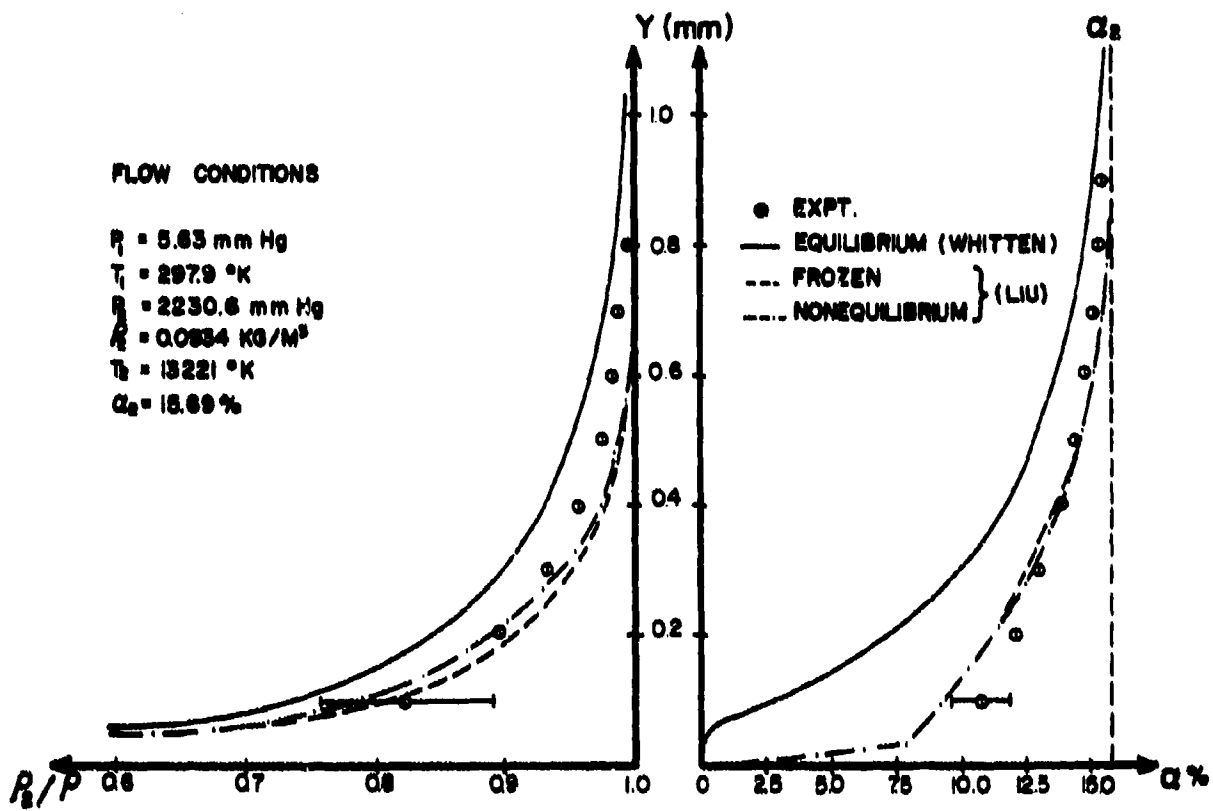
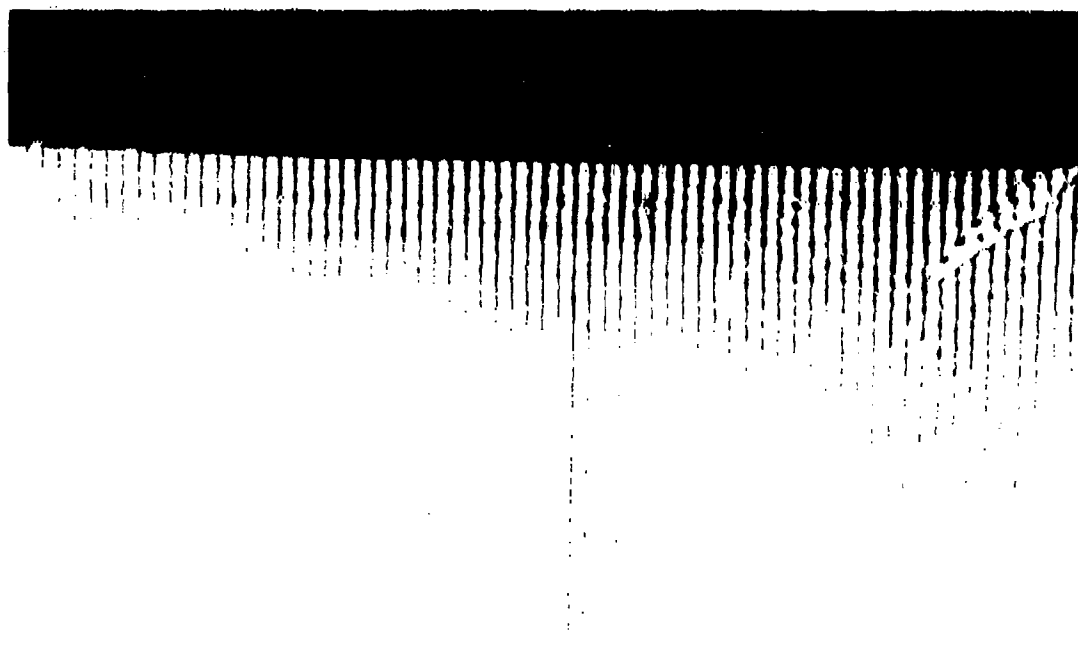
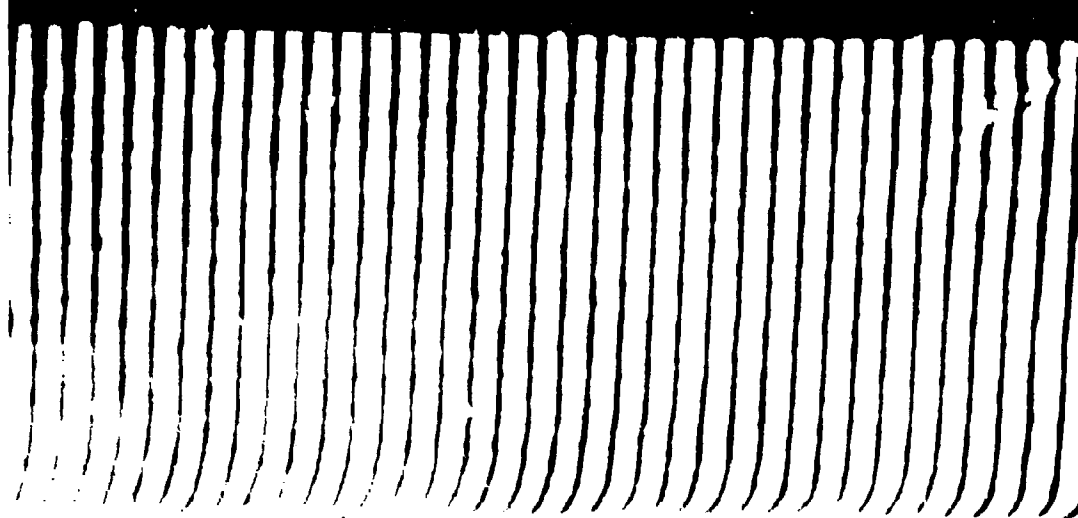


FIG. 24 INTERFEROGRAMS OF BOUNDARY LAYER HEATED SHOCK,  $\text{H}_2 + \text{He}/\text{Ar}$  TRAVELLING (TO  
RIGHT) INTO ARGON,  $P_1 = 5.22$  TORR.

627

FIG. 25 BOUNDARY LAYER DENSITY AND DEGREE OF IONIZATION PROFILES 3.75 cms. BEHIND SHOCK,  $M_s = 16.50$





Reproduced from  
best available copy.

FIG. 26 FLOW INTERFERENCES IN THE BOUNDARY LAYER BETWEEN 18 AND 20 CMS BEHIND  
SHOCK  $M_\infty = 10,40$  TRAVELING (TO RIGHT) INTO ARGON.  $P_1 = 5.10$  TORR.

FIG. 27 BOUNDARY LAYER DENSITY AND DEGREE OF IONIZATION PROFILES  
20.0 cms. BEHIND SHOCK,  $M_\infty = 16.49$

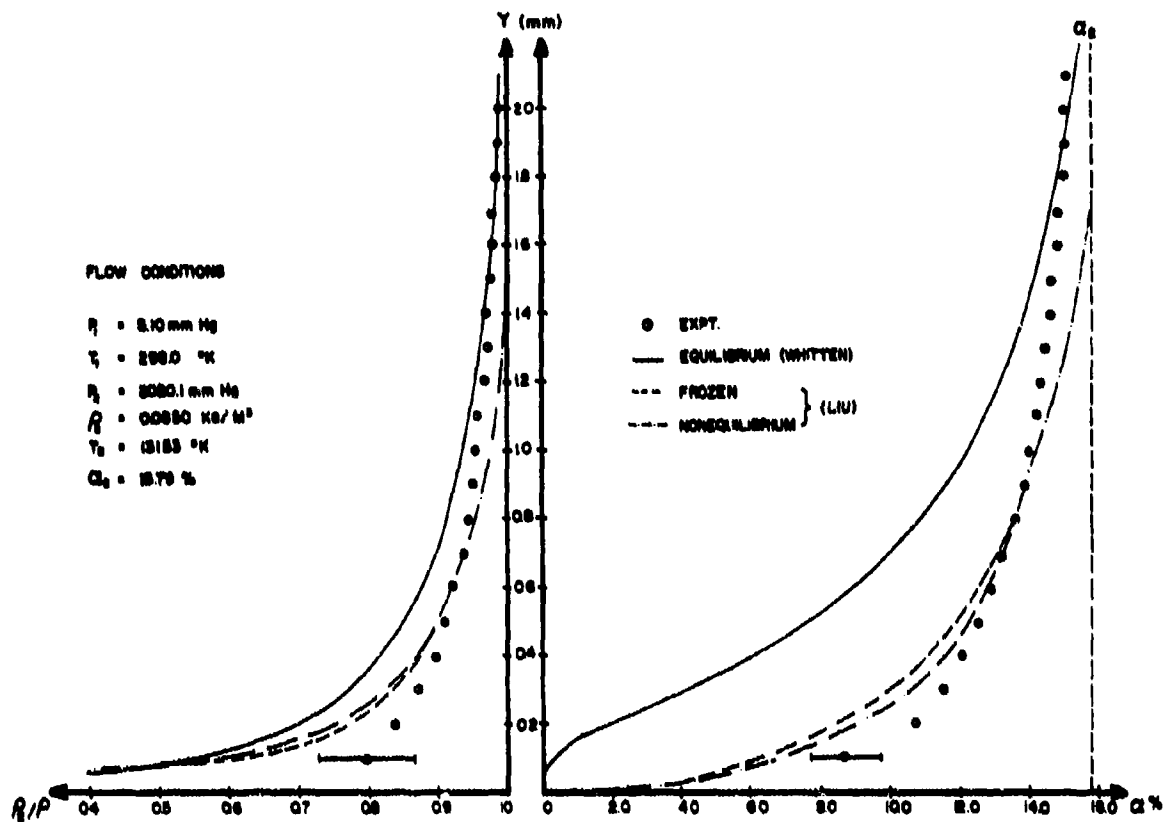
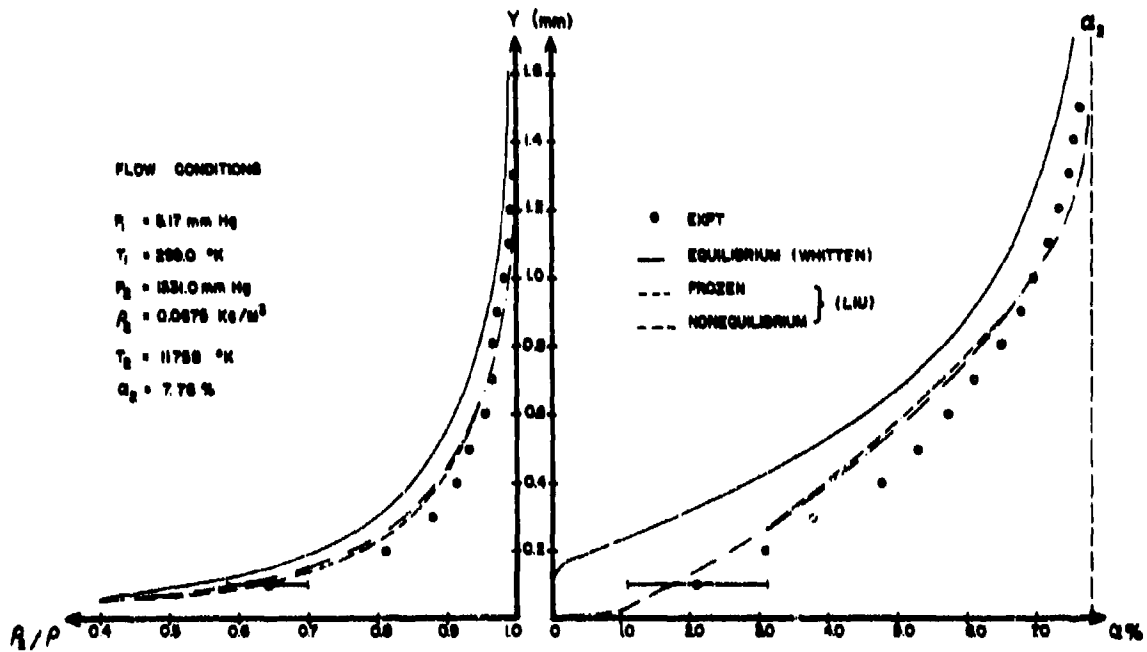
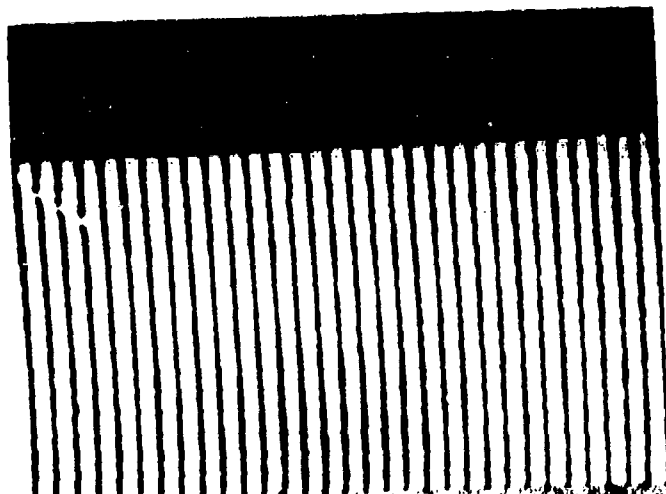
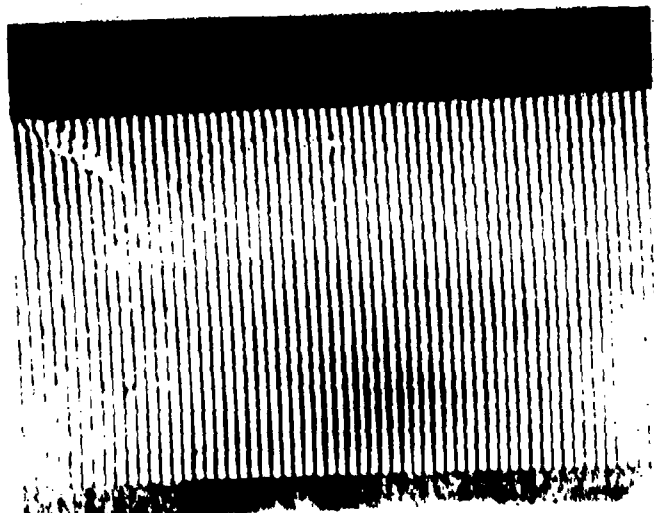


FIG. 28 BOUNDARY LAYER DENSITY AND DEGREE OF IONIZATION PROFILES  
12.0 cms. BEHIND SHOCK,  $M_\infty = 13.56$





$\lambda_1 = 6943 \text{ \AA}$



$\lambda_2 = 3471.5 \text{ \AA}$

FIG. B1 PRE - RUN POLAROID SNAPSHOTS

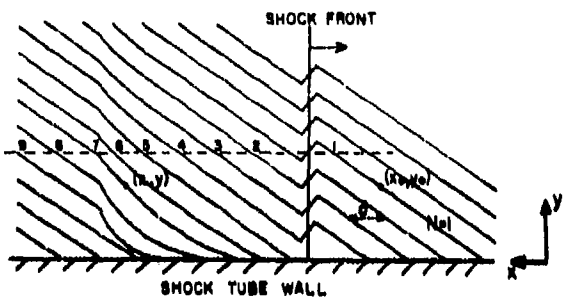


FIG. C1 SHOCK WAVE FRINGE SKETCH

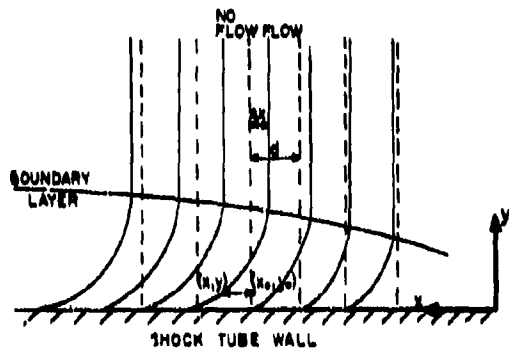


FIG. C2 BOUNDARY LAYER FRINGE SKETCH

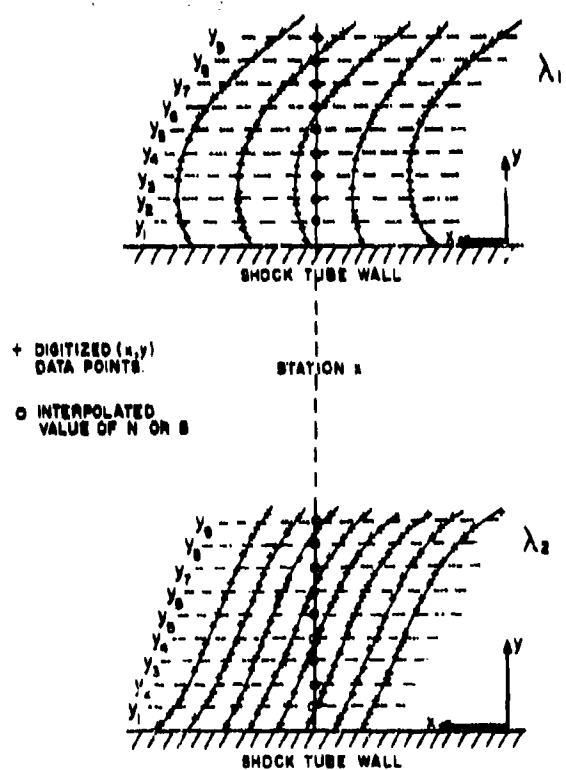


FIG. C3 INTERPOLATION SCHEME